Quantitative Acoustic Emission Monitoring of Fatigue Cracks in Fracture Critical Steel Bridges

FINAL REPORT
January 2014

Submitted by:

Thomas Schumacher, PhD, PE
Assistant Professor

Jennifer Righman McConnell
Associate Professor

Lassaad Mhamdi, PhD Candidate
Graduate Research Assistant

Shafique Ahmed, PhD Student
Graduate Research Assistant

Center for Innovative Bridge Engineering
Civil and Environmental Engineering
University of Delaware
301 DuPont Hall
Newark, DE 19716

External Project Manager
Oregon Department of Transportation
Steven C. Lovejoy, PhD, PE

Disclaimer Statement

1. Report No. CAIT-UTC-007	2. Government Accession No.	3. Recipient's Catalog No.	
4. Title and Subtitle **Quantitative Acoustic Emission Monitoring of Fatigue Cracks in Fracture Critical Steel Bridges**		5. Report Date January 2014	
		6. Performing Organization Code CAIT/Univ. of Delaware	
7. Author(s) Thomas Schumacher, PhD, PE Jennifer Righman McConnell, PhD Lassaad Mhamdi, PhD Candidate Shafique Ahmed, PhD Student		8. Performing Organization Report No. CAIT-UTC-007	
9. Performing Organization Name and Address Center for Innovative Bridge Engineering Civil and Environmental Engineering University of Delaware 301 DuPont Hall Newark, DE 19716		10. Work Unit No.	
		11. Contract or Grant No. DTRT12-G-UTC16	
12. Sponsoring Agency Name and Address Center for Advanced Infrastructure and Transportation Rutgers, The State University of New Jersey 100 Brett Road Piscataway, NJ 08854		13. Type of Report and Period Covered Final Report 08/31/2012 to 01/31/2014	
		14. Sponsoring Agency Code	
15. Supplementary Notes U.S. Department of Transportation/Research and Innovative Technology Administration 1200 New Jersey Avenue, SE Washington, DC 20590-0001			

16. Abstract

The objective of this research is to evaluate the feasibility to employ quantitative acoustic emission (AE) techniques for monitoring of fatigue crack initiation and propagation in steel bridge members. Three A36 compact tension steel specimens were tested in the laboratory according the ASTM E647. AE sensor networks were deployed and recorded AE during the fatigue-type loading. Noise from the load application points represented a significant challenge. However, a number of events could be located and for a selected few a moment tensor inversion (MTI) was performed. Despite the challenges, the methodology has been completely established and evaluated, and can be used in future testing.

17. Key Words Fatigue cracks, acoustic emission monitoring, steel, moment tensor inversion		18. Distribution Statement	
19. Security Classification (of this report) Unclassified	20. Security Classification (of this page) Unclassified	21. No. of Pages 47	22. Price

Form DOT F 1700.7 (8-69)

ACKNOWLEDGMENTS

TABLE OF CONTENTS

LIST OF FIGURES

LIST OF TABLES

DESCRIPTION OF THE PROBLEM

Despite decades of active research on the topic of fatigue cracks in steel bridges [1, 2], this remains a common problem [3-5]. With the increasing use of skewed and curved bridges, and the aging of the existing population of this bridge type, distortion-induced fatigue in particular is a growing problem [6-8]. Similarly, there are ongoing concerns regarding fatigue cracks in fracture critical bridge members, which can have disastrous consequences to the infrastructure and public safety. One common solution to stop a detected crack is to drill a so-called crack-stop hole at the end of a crack. However, the optimum size for this hole has not been entirely certain, as the minimal size to ensure a crack is indeed locked was recently reevaluated [9]. Furthermore, detecting fatigue cracks can be difficult because of their small size and tendency to develop in locations that are difficult to inspect such as gusset plate connections or web gaps [3].

> **The objective of this research is to evaluate the feasibility to employ quantitative acoustic emission (AE) techniques for monitoring of fatigue crack initiation and propagation in steel bridge members.**

Because detecting fatigue cracks can be difficult, methods for stopping fatigue cracks can be uncertain, and questions remain in understanding the micromechanics of fatigue crack propagation [10]. There is the potential for these situations to be better understood and remedied through the application of a promising technique that has been applied for a variety of applications: acoustic emission (AE) monitoring [11]. AEs are the result of sudden strain releases within a body and directly related to energy release due to fracture processes. The method is thus especially well-suited to monitor crack initiation and progression and could provide real-time feedback of fracture critical details, for example, on steel bridges. Whereas qualitative AE methods have been explored and proposed for steel fatigue crack monitoring [12-20], very few attempts have been made to employ quantitative AE methods [21]. Quantitative AE methods attempt to explain the source mechanisms employing a sensor network [11]. Most quantitative methods are adapted from seismology [22] due to the similar nature, except for scale, of AE and earthquakes. Qualitative methods on the other hand aim at establishing statistical relationships on a per-sensor basis [11]. With the recent availability of high-fidelity AE sensors, quantitative AE analysis methods have finally become a feasible means for monitoring of fracture processes.

APPROACH

The analytical approach is based on quantitative, or signal-based, AE monitoring [11]. The method is especially well-suited to monitor crack initiation and progression and can provide quantitative real-time feedback of fracture critical details, for example, on steel bridges. For this project, an event-based methodology was implemented where AE events are formed first, followed by the employment of an algorithm that estimates AE event source location coordinates. Ultimately, a moment tensor analysis (MTI) to predict the source mechanism for each event was used [23].
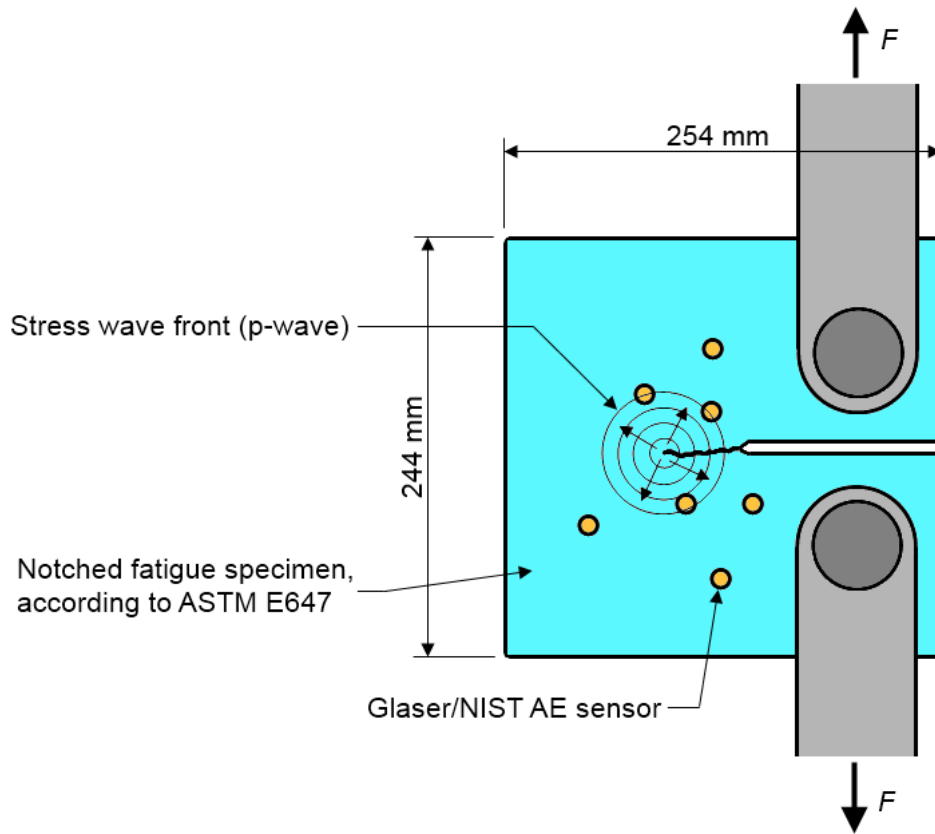
Figure 1. Conceptual illustration of the test setup.

In order to evaluate and implement the proposed analysis techniques, the methodology was first evaluated on a steel cylinder using artificially generated AE sources. Subsequently, a series of notched fatigue specimens were fabricated, loaded, and tested in the laboratory according to ASTM E647 [24], which gives the standard "Mode 1" fatigue loading protocols. Figure 1 shows a conceptual illustration of the approach. Three compact tension (CT) specimens manufactured from A36 steel, which is applicable to older bridges more susceptible to fatigue, were fabricated. A sensor network consisting of ten high-fidelity Glaser/NIST-type AE sensors [25] was deployed to capture sudden energy releases, i.e. AE from crack initiation and progression.

METHODOLOGY

Acoustic emission (AE) monitoring

In order to evaluate the feasibility of AE monitoring for fatigue crack detection, a number of algorithms had to be developed first. Subsequently, the required steps to perform quantitative AE analyses are described in detail.

Preliminary Laboratory Study

In order to establish basic data acquisition settings for application on steel structures, a preliminary experiment was performed as shown in Figure 2 (a). Nine high-fidelity Glaser/NIST point-contact piezoelectric AE sensors (as shown in Figure 2 (b)) were mounted on the surface of a steel cylinder (Diameter x height = 6 x 12 inches) and connected to the data acquisition system.
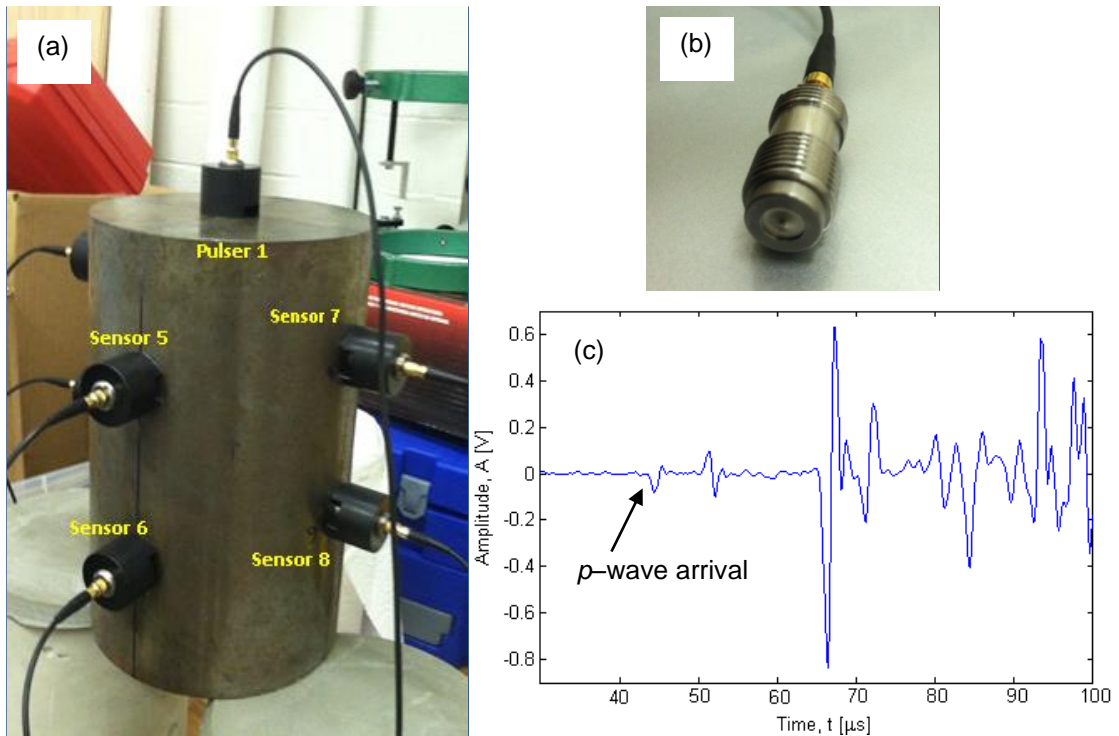
Figure 2. Preliminary test on a solid steel cylinder: (a) experimental setup, (b) view of high-fidelity AE sensor, and (c) example AE waveform with labeled *p*-wave arrival.

p-Wave Arrival Time Picking

Figure 2 (c) shows a typical signal recorded from one sensor. The input signal for this case was created using a modified Glaser/NIST sensor (denoted *Pulser 1*) that can be actuated by a waveform generator using a Morlet-type waveform. As can be observed, the recorded signal

clearly shows the arrival of the first wave mode, the compression, or *p*-wave. The first step in quantitative AE analysis is to pick these *p*-wave arrivals since they represent the first undisturbed piece of information that arrives at a sensor. Subsequent modes such as the shear (*s*-) wave or the surface (*R*-) wave can be difficult to observe and often contain boundary reflections. An algorithm was implemented in MATLAB to (1) pick the *p*-wave arrivals based on the Akaike Information Criterion (*AIC*) [26] and (2) estimate AE source locations based on Geiger's method [27]. The *p*-wave picker that was developed for this research consists of two iterations of the *AIC* function as illustrated in Figure 3. The minimum value of the second AIC function (purple vertical marker) represents the final estimate for the *p*-wave arrival. The idea of using the AIC criterion has been used in the AE community for a few years and shown to perform more accurately and reliably compared to other picking schemes [28].
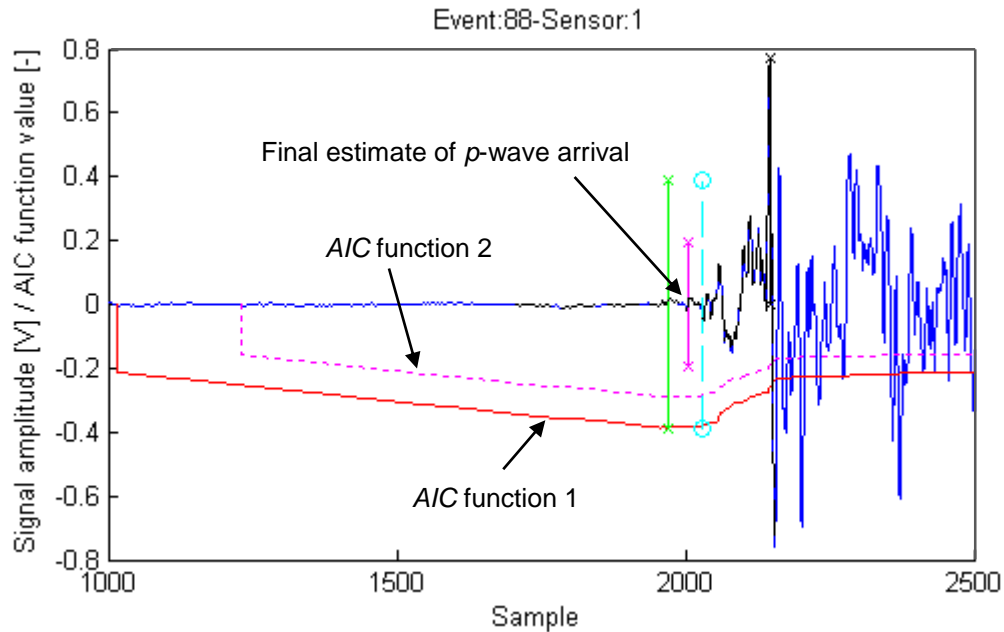
Figure 3. Example of picked *p*-wave arrival from signal during preliminary tests. The green, blue, and purple vertical makers represent initial threshold exceedance-based pick, first *p*-wave arrival estimate using *AIC* function 1, and final *p*-wave arrival estimate using second iteration (AIC function 2), respectively.

Once all the *p*-wave arrivals are picked accurately (as illustrated in Figure 3), AE events are formed. An event is a group of AE signals that are associated with a common source, i.e. depending on the sensor network they must arrive at every sensor within a limited time. Since our data acquisition system allows for event-based triggering and recording, events were discriminated and stored as such by the data acquisition system. Next, the source origin can be estimated using an iterative triangulation scheme.

Estimation of AE Source Locations

To date, earthquake epicenter locations are estimated in a reliable manner, which works for AE as well, using Geiger's method [27]. An example of an AE event, which is a collection of AE signals that arrive within a certain time window and can therefore be associated with a physical cause, is illustrated in Figure 4. When the source location is known, such as in the case of a pencil lead break, the *p*-wave velocity can be estimated easily using the distance between the source and the sensors and the arrival times of the *p*-wave. As can be seen in Figure 4, the calculated value is approximately 5800 m/s, which would be expected for regular structural steel.
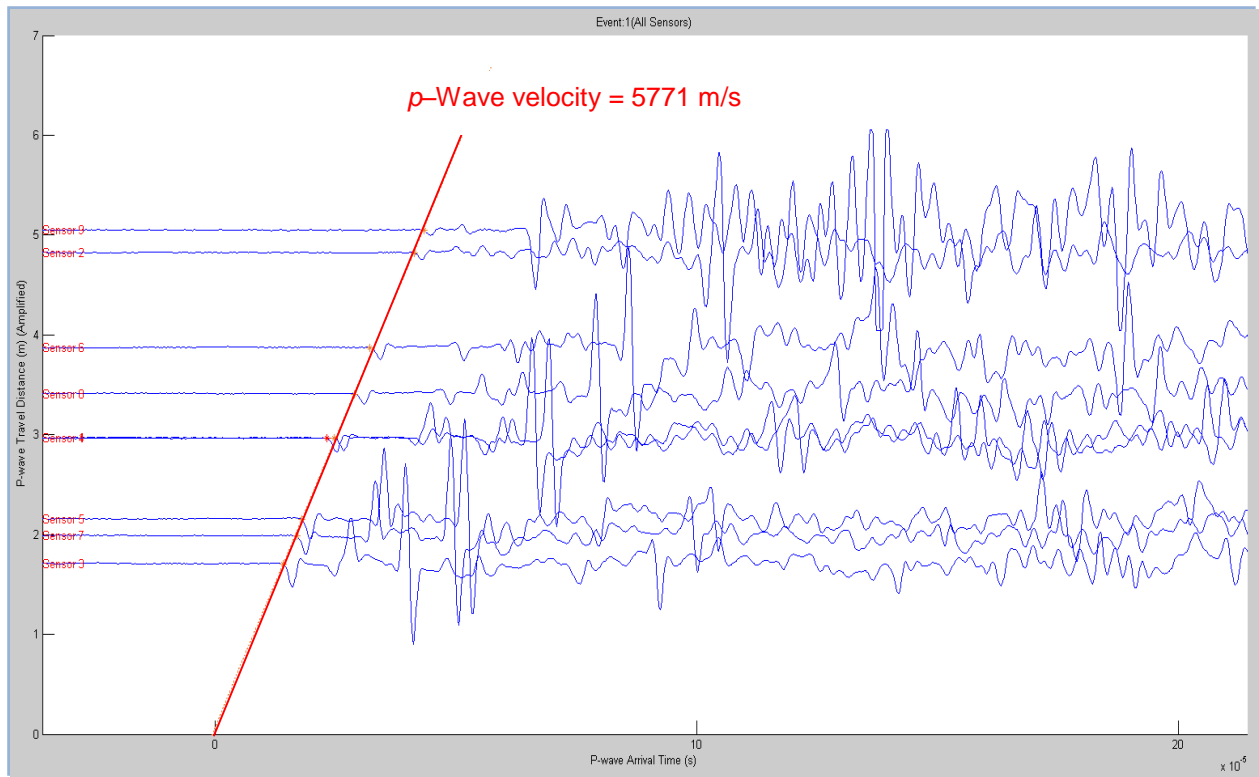
Figure 4. Example of recorded AE signals from steel cylinder. The x-axis shows time and the y-axis the calculated distance from the source each of the sensors. The red line is a linear curve fitted through the arrival times of the *p*-wave such that the slope represents the *p*–wave velocity.

Geiger's source location method [27] requires at least four signals to estimate three-dimensional source locations: three spatial coordinates and the event time. A detailed description of this source location scheme as well as a few derivatives can be found in Ge's paper [29]. The fundamental assumptions are that the medium is elastic, heterogeneous, and isotropic. The governing equation used in Geiger's method is the so-called arrival time function:

$$f_i(x) = f_i(x_0, y_0, z_0, t_0) = t_0 + \frac{\sqrt{(x_i - x_0)^2 + (y_i - y_0)^2 + (z_i - z_0)^2}}{c_p} \qquad \textbf{(Eq. 1)}$$

The subscript 'i' denotes the index of the AE sensor deployed in the network where x_i, y_i, z_i represent the spatial coordinates and t_i is the p-wave arrival time. t_0 denotes the source event time (time at which the elastic wave, or AE, initiated), and x_0, y_0, z_0 represent the spatial coordinates of the source. The travel paths between source and sensors are assumed to be straight, having a p-wave velocity, c_p. In all source location estimations, a p-wave velocity of 5800 m/s was used. The goal of the method is to minimize the residuals, r between calculated, subscript 'c' and observed, subscript 'o' arrival time at each sensor:

$$r_i = \min(t_{i,o} - t_{i,c}) \qquad \textbf{(Eq. 2)}$$

This is done by solving this inverse non-linear problem iteratively. Starting from a trial solution, a first set of source coordinates is calculated using Equation 1. The arrival times calculated for all sensor locations are then compared to the observed arrival times and sensor residuals are computed according to Equation 2. A correction vector is then computed based on the first derivatives of the linearized arrival time function (Equation 2) using a least squares approach and added to the calculated source location parameters [29]. The process is repeated until a predefined stopping criterion is fulfilled. This iterative algorithm was implemented in MATLAB and was applied to all the AE events in our experiments.

Uncertainties in the actual p-wave speed, travel paths in cracked heterogeneous and anisotropic materials, and the errors in the picking of the arrival times from the AE signals introduce errors in the results [30]. If more than five AE signals are available, the system of equations is over-determined (five or more equations and only four unknowns) and the covariance matrix of the solution using the least-squares method can be computed. The principal standard deviations, σ_1, σ_2, σ_3, along with their direction cosines can then be obtained by simply solving for the eigenvalues and eigenvectors of the covariance matrix. These standard deviations are a measure of inconsistency in the observed arrival times and not the absolute error associated with a certain location result. For example, systematically delayed arrival times would remain unrevealed [31]. An example of how the source locations can be visualized is given in Figure 5. Results are visualized using the mean solution and the calculated principal standard deviations shown in red, blue, and green. The mean solution lies at the intersection of these lines. The size of the ellipsoids is a direct measure of the variance in the solution, i.e. the smaller the ellipsoid the more consistent the solution. For sources where the origin is known, for example from pencil lead breaks applied to the surface, the prediction error, ε can be calculated.
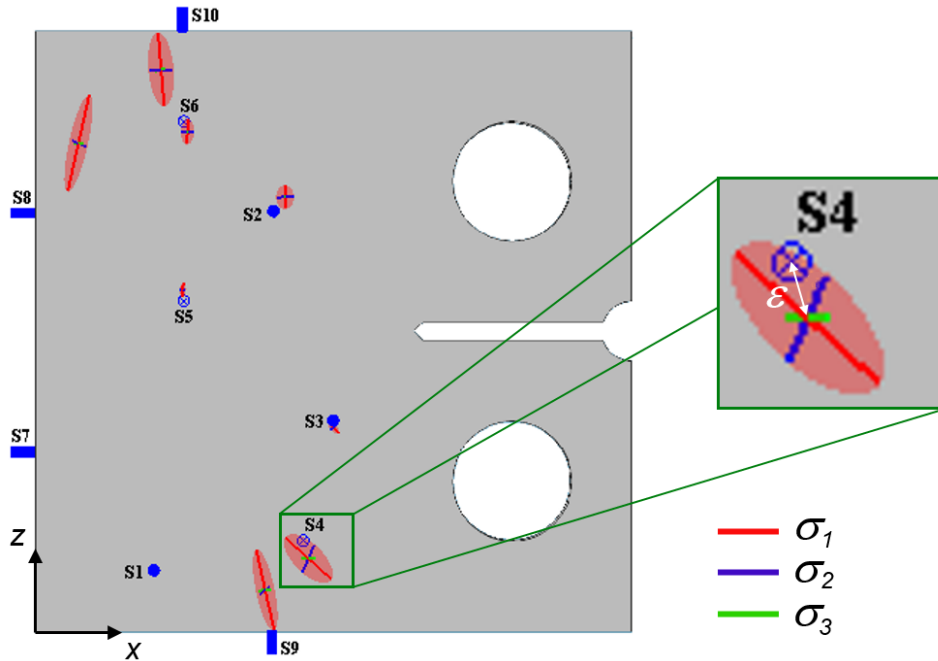
Figure 5. Example of results obtained from source location algorithm (Specimen 1). The source was pencil lead breaks that were applied at each sensor location (denoted S1 through S10) on the opposite face of the steel plate.

In order to establish the location accuracy, pencil lead breaks were performed on both Specimen 1 and 2 at a few selected locations. Table 1 shows a summary of actual and predicted locations as well as the calculated errors, ε. Two error calculations were made: the first one including all coordinates (x-y-z) and the second one only two (x-z). The reason being that a sensor array on a plate-like specimen will inevitably be very sensitive for errors in the direction of the smallest specimen dimension, i.e. the specimen thickness, or y-coordinate. It can be observed that the errors in the y-direction are indeed much larger. An option could be to constrain the location results in the y-direction since the physical boundaries of the plate are known. This was not pursued at this point but will be looked at in the future. The errors are typically below 0.4 in., with a few outliers, which is reasonable given shape and size of the specimens.

Table 1. Evaluation of location accuracy using pencil lead breaks.

Specimen 1		S1	S2	S3	S4	S5	S6	S7	S8	S9	S10
Pencil lead break coordinate	x (in.)	2.00	4.00	5.00	4.50	2.50	2.50	0.50	0.50	4.00	2.50
	y (in.)	0.50	0.50	0.50	0.00	0.00	0.00	0.00	0.00	0.00	0.00
	z (in.)	1.00	7.00	3.50	1.50	5.50	8.50	4.00	8.00	0.50	9.13
Estimated location	x (in.)	-	4.19	5.00	4.58	2.48	2.55	-	0.73	3.86	2.11
	y (in.)	-	0.36	0.28	0.11	0.28	0.19	-	0.85	0.08	0.47
	z (in.)	-	7.23	3.39	1.19	5.68	8.32	-	8.13	0.67	9.36
Error, ε (in.) ⇨ x-y-z		-	0.33	0.25	0.39	0.33	0.27	-	0.89	0.23	0.65
Error, ε (in.) ⇨ x-z		-	0.30	0.11	0.32	0.18	0.19	0.26	0.22	0.46	-
Specimen 2		S1	S2	S3	S4	S5	S6	S7	S8	S9	S10
Pencil lead break coordinate	x (in.)	2.31	5.31	2.31	3.31	0.00	-	-	2.31	2.31	3.31
	y (in.)	0.00	0.00	0.00	0.00	0.25	-	-	0.50	0.50	0.50
	z (in.)	1.81	4.18	4.81	5.81	1.81	-	-	1.81	4.81	4.81
Estimated location	x (in.)	2.19	5.49	2.28	3.2.	-0.05	-	-	2.09	2.18	3.38
	y (in.)	0.71	0.07	-0.72	0.14	-0.24	-	-	0.02	-0.76	0.13
	z (in.)	1.64	4.89	4.82	5.88	1.63	-	-	1.60	4.83	4.94
Error, ε (in.) ⇨ x-y-z		0.74	0.73	0.72	0.19	0.53	-	-	0.57	1.27	0.40
Error, ε (in.) ⇨ x-z		0.21	0.73	0.03	0.13	0.19	-	-	0.31	0.13	0.14

Figure 6 shows an example of an AE event due to a pencil lead break with all individual signals recorded at each sensor.
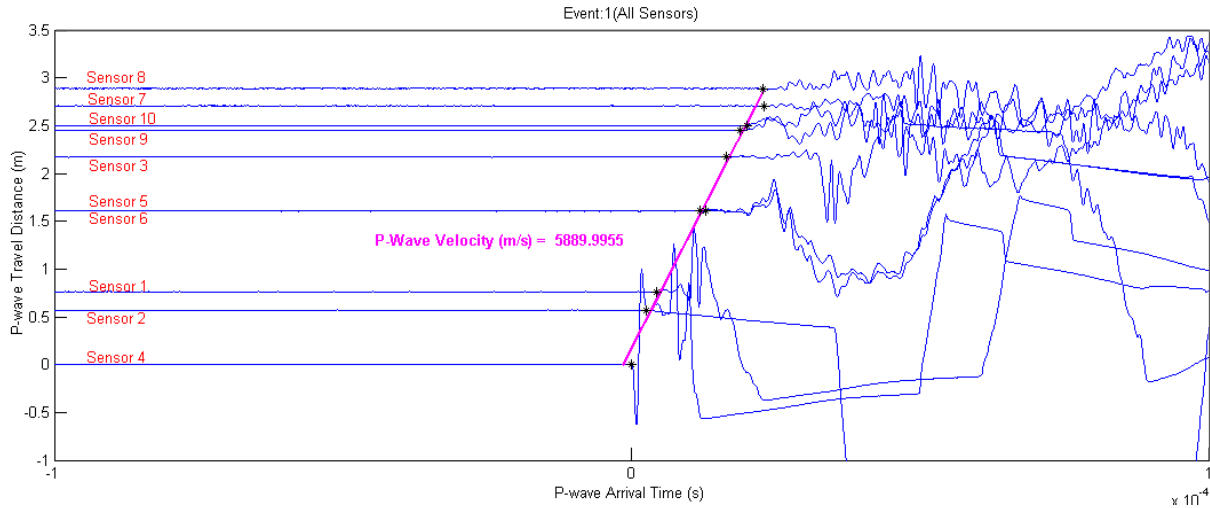
Figure 6. Example signals from a pencil lead break.

The last and final step in quantitative AE analysis is the moment tensor inversion (MTI). In this study, a tool box developed to investigate mining-induced seismicity was adapted and employed to characterize the nature of AE events [23]. The inputs needed to perform an MTI computation are (1) source location, (2) *p*-wave amplitudes, and (3) the elastic Green's Functions, which describe the wave propagation in the medium (also see Chapter *Experimental Setup*, Section *Acoustic Emission Monitoring*). The idea of a moment tensor is that a point source can be

represented by a set of 9 force couples. Due to symmetry, the off-diagonal terms of the moment tensor are the same, which reduces the number of independent terms to 6. This means that at least 6 AE signals need to be recorded in order to perform a MTI. In order to obtain stable and reliable results, and in the presence of noise, it is often required to have a higher number of signals. In our tests we typically use at least 8 sensors and we can employ up to 14. Figure 7 illustrates the moment tensor representation. Also shown are two examples of sources: (a) pure explosion (all off-diagonal terms are zero) and (b) pure shear (only two off-diagonal terms non-zero, e.g. 12 and 21). Pure tensile rupture would theoretically produce a pure explosion source and a shear source could be theoretically caused by slip or friction between two interfaces.
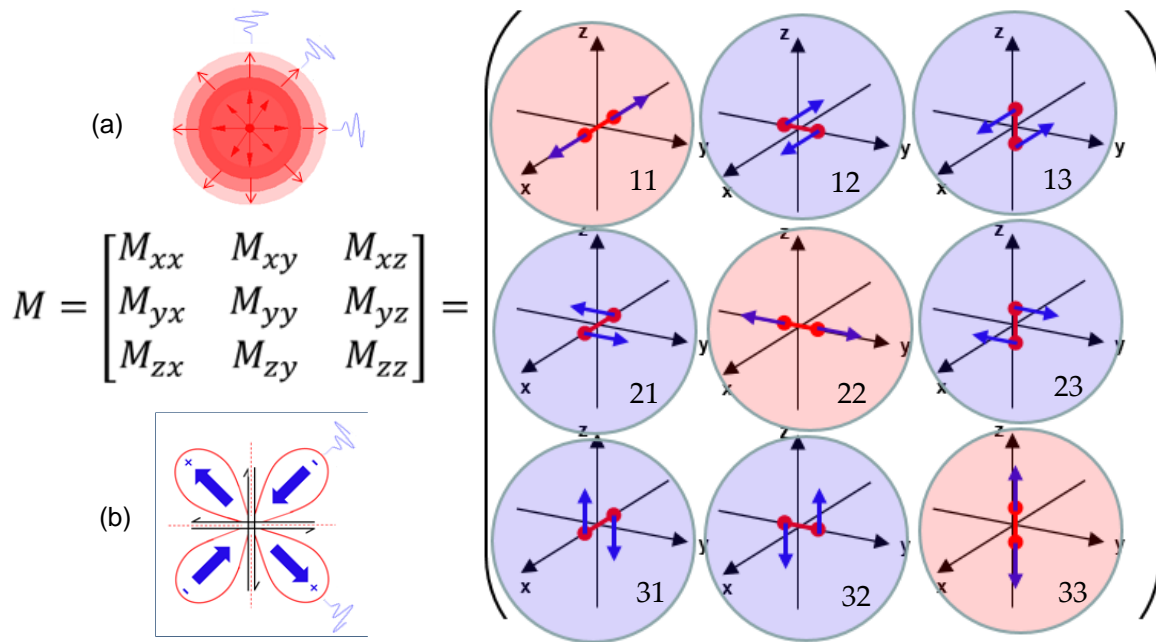
Figure 7. Illustration of the concept of a moment tensor and example sources.

The toolbox offers great flexibility and has the option to process data in several ways as summarized in Table 2. We were only able to use an absolute MTI approach since the other two require the availability of groups (or clusters) of events. A detailed description of the MTI toolbox along with an evaluation of the method applied to civil engineering materials can be found in [32].

Table 2. Overview of MTI approaches available in toolbox (Source: [32]).

	Strengths	Limitations
Absolute MTI approach	• Applied in single or sparse event situations	• Difficult to apply in non-homogeneous environments • Tedious evaluation of the Green's functions for every AE event • Requires a dense network of AE sensors • Sensitive to noise
Relative MTI approach	• Green's Functions can be estimated from a reference event, either empirically or theoretically • In special cases, the Green's functions can be eliminated analytically (no need to evaluate them) • Applied to clusters of AE events	• Requires a cluster of events, i.e. cannot be applied in single event situations • Events in the cluster must have different radiation patterns • Extremely sensitive to noise if source mechanisms of the cluster events are very similar
Hybrid MTI approach	• Capitalize on the strengths of both the Absolute and Relative MTI methods • Compensate for different types of systematic errors in the AE waveforms • Achieve accurate and robust measure of the Moment Tensor	• Require the evaluation of the Green's functions

In practicality it is expected that most AE sources will have an isotropic as well as mixed-mode components. This can be explained by the fact that steel fatigue cracks have some variability and do not produce a straight line. The solution of an MTI is typically represented by a stereograph, often referred to as *beachball*, which is the representation geoscientists use to visualize seismic events. Figure 8 illustrates the most common fracture types and their stereographic representation.
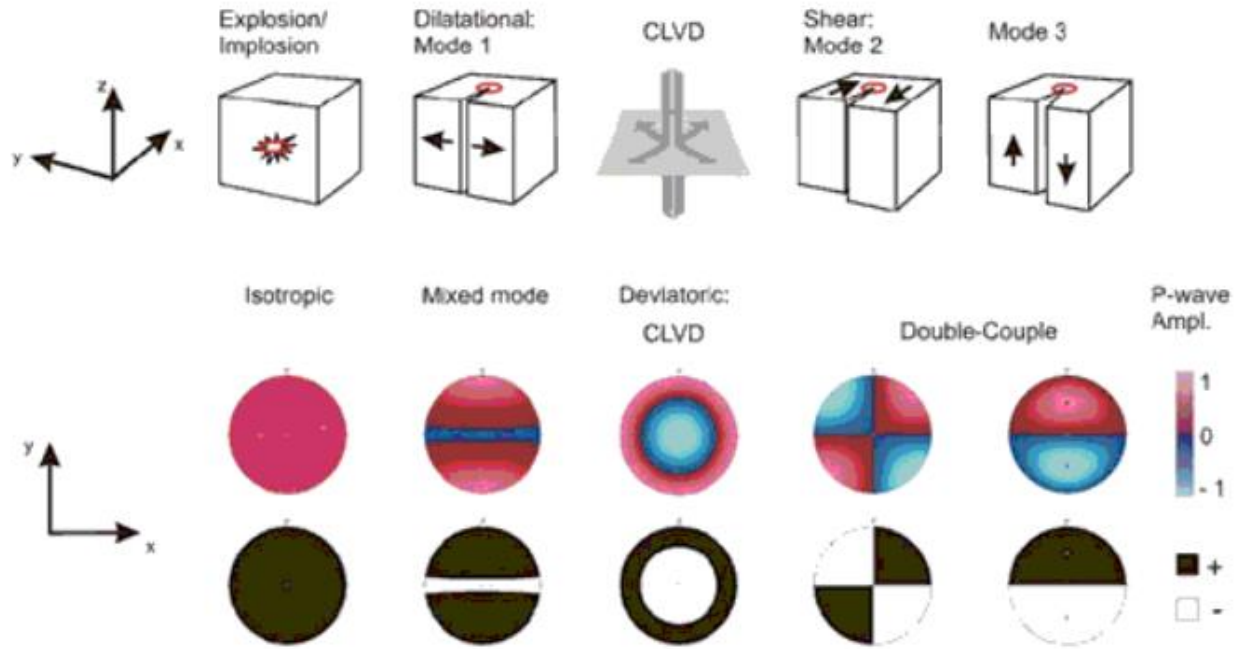
Figure 8. Stereographic representations of MTI solution (Source: [33]).

Design of Test Specimens

Three test specimens were fabricated from A36 structural steel and followed the ASTM E647 Standard. Due to the type of testing machine available, the compact tension (CT) specimen was selected with parameters $W = 8.0$ in. and milled to a thickness $B = 0.5$ in. The thickness, $B = 0.5$ in. was selected to be within the recommended range:

$$\frac{W}{20} \leq B \leq \frac{W}{4} \rightarrow \frac{8 \text{ in.}}{20} = 0.4 \text{ in.} \leq 0.5 \text{ in.} \leq \frac{8 \text{ in.}}{4} = 2.0 \text{ in.} \qquad \textbf{(Eq. 3)}$$

Specimen dimensions along with a photo are shown in Figure 9.
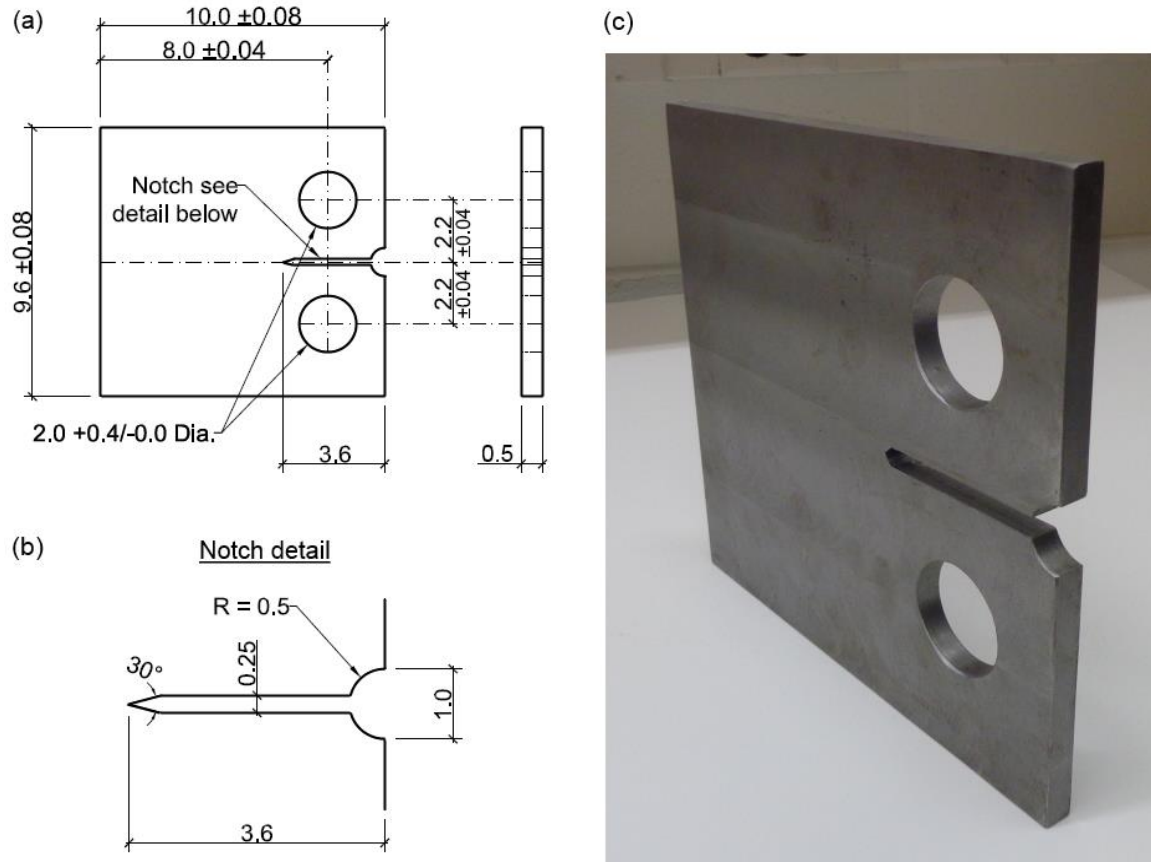
Figure 9. Design of test specimens: (a) Overall dimensions, (b) notch detail, and (c) photo of fabricated specimen. All dimensions in (inches).

Three 0.5 inch diameter circular dog bone-type coupons were fabricated and tested in tension according to ASTM A370 [34] to failure to determine actual material properties of the steel used in the CT specimens. The properties are summarized in Table 3.

Table 3. Material properties for test specimens.

	Yield stress at 0.2%	Ultimate stress	Fracture strain	Modulus of Elasticity
Coupon 1	51.8 ksi	76.0 ksi	27.0%	30,500 ksi
Coupon 2	55.6 ksi	76.1 ksi	29.9%	35,500 ksi
Coupon 3	50.6 ksi	74.4 ksi	24.4%	28,500 ksi
Mean	53.1 ksi	75.5 ksi	27.1%	31,500 ksi
C.o.V.	6.66%	1.26%	10.2%	11.5%

The estimation of fracture toughness parameters to determine the required stress levels for fatigue loading is presented in Section *Loading Protocols*.

Experimental Setup

Testing Machine and Conventional Sensors

For all experiments a 200 kip capacity Tinius Olsen hydraulic universal testing machine was used. Figure 10 shows the testing machine with the high-strength clevises designed for this project. The clevises were connected to the universal testing machine via 1 inch diameter Grade 8 threaded rods and prestressed to a level of 35 kips in order to keep extensions during the test to a minimum. A 1 inch range potentiometer was mounted to the edge near the notch opening in order to measure displacements across the notch.
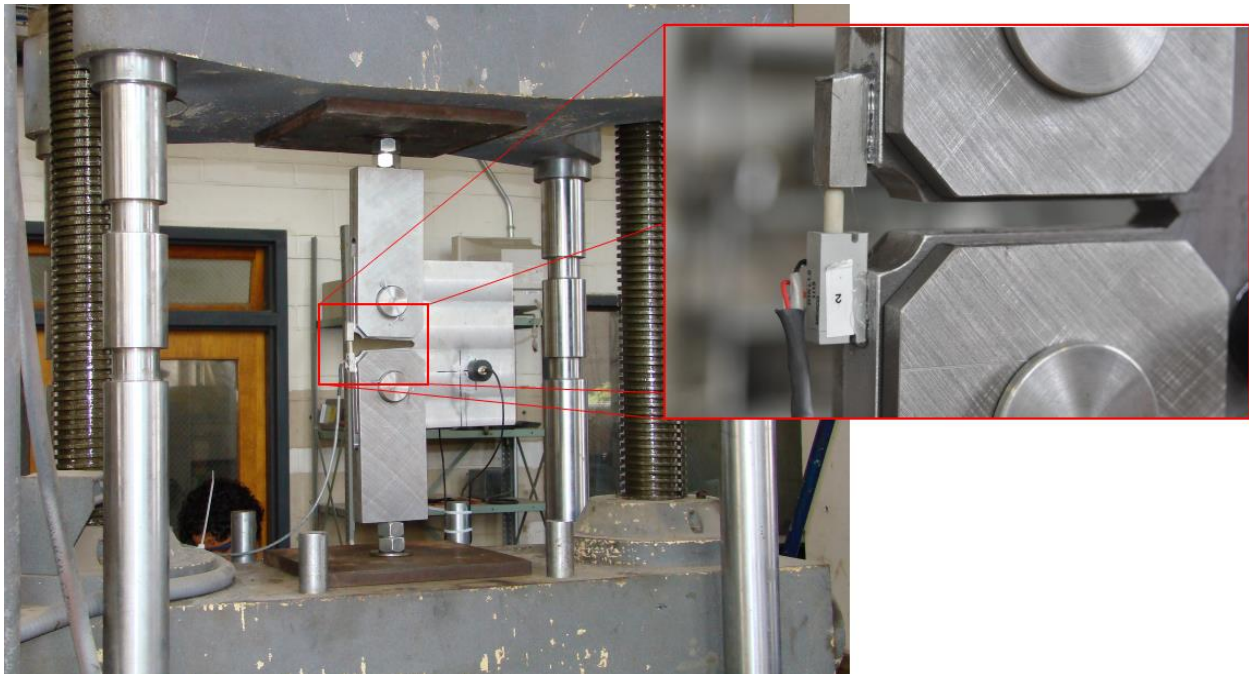
Figure 10. Universal testing machine with high-strength clevises and CT specimen during testing. The insert shows the potentiometer used to measure notch opening displacement.

The Tinius Olsen universal testing machine is programmable via a connected computer and the loading protocols are described in detail in Section *Loading Protocols*.

Acoustic Emission Monitoring

The components required to collect AE data along with key characteristics of the measurement system are summarized in Table 4. The AE measurement process can be described in mathematical form as a series of transmission functions convolved with the source signal:

$$R(t) = S(t) * TF_M(t) * TF_S(t) * TF_R(t)$$

(Eq. 4)

where $R(t)$ is the recorded signal, $S(t)$ the AE source signal, $TF_M(t)$ the elastic Greens' Functions which describe the wave propagation (and theoretically need to include inhomogeneities and isotropic behavior) of the medium, $TF_S(t)$ the sensor response characteristics, and $TF_R(t)$ the characteristics of the data acquisition system (e.g. used filters, response characteristics of amplifiers, etc.) [35]. Components with a flat frequency response (= high-fidelity devices) can be neglected, i.e. there transmission functions can be set to a constant of 1. In summary, this relationship highlights the need to carefully consider each component of the measurement process and how it affects the actual AE source signal. In other words, what is displayed on the screen may only remotely reflect the actual source characteristics.

Table 4. Components and key characteristics of AE data acquisition system.

Element	Key Characteristics
Glaser/NIST sensors, KRN Services, Inc.	▪ Point-contact sensor ▪ Conical piezoelectric crystal with built-in JFET ▪ High-fidelity broad-band response ▪ High sensitivity
Pre-amplifiers, KRN Services, Inc.	▪ Wide-band amplification (up to 2MHz) ▪ Input noise less than 10 mV ▪ Output voltage up to 22 V
Analog filters, Krohn-Hite Corp.	▪ 15 channels ▪ 20 kHz high-pass 8-pole Butterworth filter
Data Acquisition System, Elsys Instruments, LLC	▪ 16 channels with 14-bit @ 40 MHz/16-bit @ 5 MHz ▪ Up to 128 MS acquisition memory per channel ▪ Flexible parallel triggering mode using all channels for event-based recording ▪ LAN Ethernet connection
Personal Computer, Dell Corp.	▪ Windows 7 Enterprise ▪ Intel® Core™ i7 CPU 2.93 GHz Processor ▪ 8 GB RAM

Typical AE sensors work based on the piezo-electric effect, i.e. when a piezo-electric material is deformed it produces an output voltage proportional to the experienced deformation. Most commonly, lead zirconium titanate (PZT) is used for the sensing element. For all our experiments we used Glaser/NIST sensors. These can be absolutely calibrated [25] and shown to have a relatively flat response (within 3 dB) over a frequency response from 20 kHz to 1 MHz with respect to displacement. Figure 11 shows the sensor and its basic response characteristics. These sensors were selected specifically because of their high-fidelity response characteristics which would ensure that quantitative procedures such as moment tensor inversion (MTI), which rely on unbiased measurements, would be applicable.
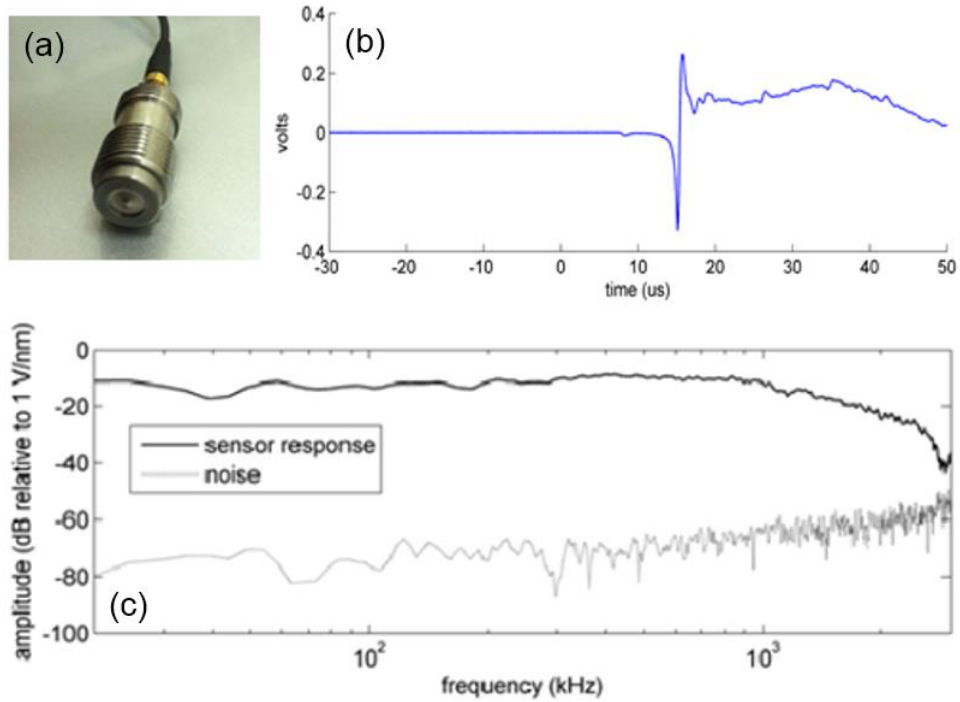
Figure 11. The Glaser/NIST point-contact sensor: (a) Photo of the sensor connected to cable, (b) typical time-history response, and (c) typical spectral response obtained from the fracture of a radially loaded glass capillary tube (Data provided by KRN Services, Inc.).

Figure 12 shows an example of the deployed AE sensor network. For Specimen 0, only two sensors were deployed (see Figure 9) as the goal for this preliminary test was to establish data acquisition parameters and evaluate the basic response of the specimen. Basic parameters determined include trigger criteria and waveform duration and found to be ± 0.1 V and 0.5 ms, respectively. On Specimens 1 and 2, sensor networks consisting of 10 sensors were deployed and their locations are listed in Table 5. The orientation of the coordinate system is shown in Figure 12.

Figure 12. Back (left photo) and front (right photo) side of Specimen 1 with AE sensor network. The white arrows depict the coordinate system used for the sensors.

Table 5. Sensor locations for Specimens 1 and 2.

Specimen 1	S1	S2	S3	S4	S5	S6	S7	S8	S9	S10
x (in)	2.00	4.00	5.00	4.50	2.50	2.50	0.00	0.00	4.00	2.50
y (in)	0.00	0.00	0.00	0.50	0.50	0.50	0.25	0.25	0.25	0.25
z (in)	1.00	7.00	3.50	1.50	5.50	8.50	4.00	8.00	0.00	9.63
Specimen 2	S1	S2	S3	S4	S5	S6	S7	S8	S9	S10
x (in)	4.31	5.31	2.31	3.33	4.31	4.31	0.00	2.31	5.31	4.31
y (in)	0.00	0.00	0.00	0.50	0.50	0.50	0.25	0.25	0.25	0.25
z (in)	3.81	5.81	7.81	3.83	3.81	1.81	4.81	9.63	9.63	0.00

Figure 13 shows the data acquisition system and pre-amplifiers used for all experiments. Pre-amplifiers are used to intensify the small voltage outputs generated by the AE sensors. 20 kHz analog high-pass filters (hardware not shown) were employed to suppress low frequency events that could potentially be generated by the test setup. The high-speed data acquisition system digitizes the amplified and filtered signals and stores the waveform data. One specialty of an AE data acquisition system is that it offers event-based recording where several sensors record simultaneously when a pre-defined trigger criteria is fulfilled. The analysis of the signals (and events) was performed using a standard Windows PC and the technical computing software MATLAB.

Figure 13. Data acquisition (bottom box) with 12 and 4 channel pre-amplifiers (middle and top boxes, respectively).

Loading Protocols

Preliminary test: Specimen 0

This specimen was loaded in tension until failure in one step. The objective of this preliminary test was to evaluate the design of the test setup, including the performance of the clevises, and to establish parameters for the recording of AE data. In order to keep the test simple, only two AE sensors were mounted, just below where a crack was expected to propagate, one on each side of the specimen. Pencil lead breaks were performed on the surface of the specimen prior to the test to ensure the sensors are coupled properly and show similar amplitude response. Figure 14 illustrates the test setup.
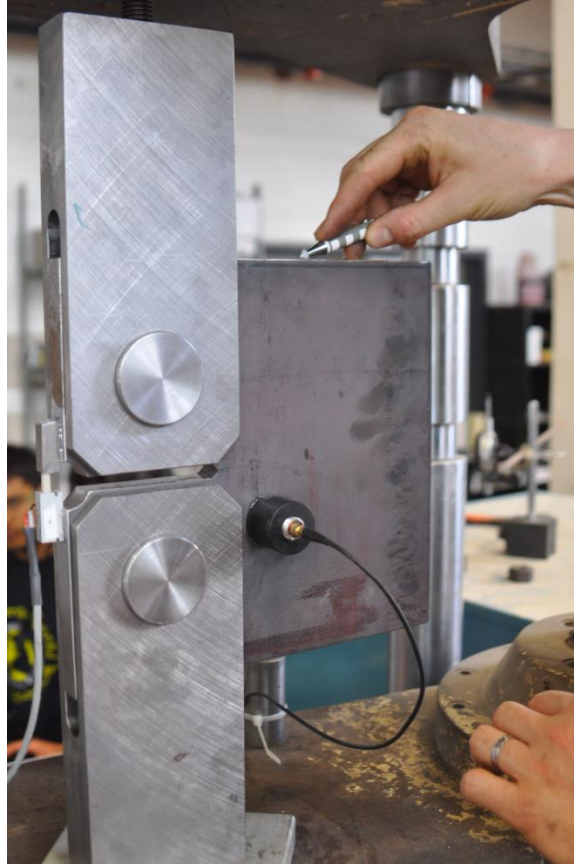
Figure 14. Specimen 0 prior to test, pencil lead breaks applied to verify sensor response.

The specimen was loaded to a total tension load of 60 kip over a period of 2500 s. The actual load-displacement curve as well as the measured AE event rate are presented in discussed in Chapter *Findings*, Section *Specimen 0*.

Specimen 1 and 2

The loading protocols for the fatigue testing were based on two primary constraints. The first of these was adherence to ASTM E647 [24], which details the standard test method for the measurement of fatigue crack growth rates. This is desirable to ensure that fatigue cracking initiates and propagates in a controlled manner which can be reproduced in later work. The second of these were the laboratory constraints and logistics of performing the fatigue testing. Specifically, due to the significant number of cycles and thus relatively long duration needed for fatigue testing, it was desirable to minimize this time to a reasonable extent (such that active testing time for each specimen was less than 2 weeks at the 0.25 Hz maximum frequency of the equipment available at the time).

Given these constraints, the primary loading protocols to be determined where minimum and maximum loadings (which taken together give the loading range ΔP), the loading rate, and the number of expected cycles. The starting point for selecting values for these parameters was Equation 5, which can be expanded to Equation 6 [36]:

$$\frac{da}{dN} = C\left(\Delta K_I\right)^m \qquad \text{(Eq. 5)}$$

$$N = \int_{EIFS}^{a_f} \frac{da}{C\left[\frac{\Delta P\,(2+\alpha)\left(0.886+4.64\alpha-13.32\alpha^2+14.7\alpha^3-5.6\,\alpha^4\right)}{C}\right]^m} \qquad \text{(Eq. 6)}$$

In Equation 5, $\frac{da}{dN}$ = crack growth rate while C and m are the Paris coefficients, which are tabulated for different steels including A36 steel which is used in this research on Page 239 of [37], and ΔK_I is the stress intensity range. In Equation 6, $EIFS$ = equivalent flow size, a_f = final crack length, $\Delta P = P_{max} - P_{min}$ = load amplitude, B = specimen thickness, W = specimen width, a = crack length, and = $\frac{a}{W}$.

Equations 5 and 6 show that the stress intensity (K_I) is directly related to crack length and loading. Equation 7 specifically defines this relationship for the compact tension (CT) specimens used in this work [13, 36, 38, 39]:

$$K_I = \frac{P}{BW^{1/2}} \frac{2+\alpha}{(1-\alpha)^{3/2}} \left(0.886 + 4.64\alpha - 13.32\alpha^2 + 14.7\alpha^3 - 5.6\,\alpha^4\right) \qquad \text{(Eq. 7)}$$

In Equation 7, P = applied load, B = thickness of the specimen, W = specimen width, and $\alpha = a/W$. Thus, only the loading and the crack length are influential variables affecting stress intensity for the fixed specimen geometry. Figure 15 plots this relationship between crack length and stress intensity for the CT specimens used in this work when subjected to different loading ranges. This data is viewed relative to the assumed fracture toughness of the specimens, which was 110 MPa $\sqrt{m}$, a value within the range of values possible for the A36 steel from which these specimens are fabricated. The first crack will theoretically occur when K_I reaches the fracture toughness (or when K_I reaches K_{IC}). Figure 15 shows that 28 kips is the maximum loading that can be used that allows the fracture toughness to intersect with the stress intensity predicted by Equation 7. Thus, 28 kips was selected as the targeted P_{max}, and was typically used as shown by Table 6, which details the loading protocol used for Specimen 1. Specimen 2 followed a similar loading protocol, but P_{max} as high as 35 kips was used at the latter stages of testing this specimen.
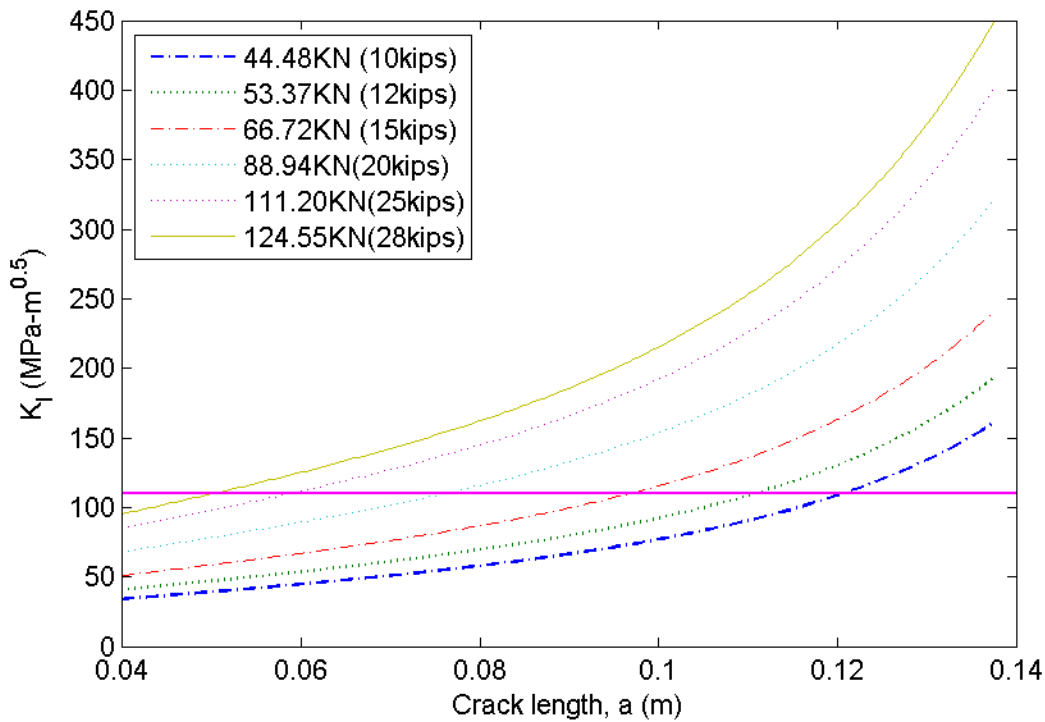
Figure 15. Relationship between crack length and stress intensity.

Figure 15 also provides a basis for evaluating the extent to which the loading protocols produced a response consistent with theoretical expectations. Specifically, again taking the assumed fracture toughness of 110 MPa $\sqrt{m}$, a final crack length can be predicted as 50.2 mm. This value can be compared to the actual crack length observed during the testing, which is composed of three distinct regions. The initial crack has a length of 40 mm. Figure 16 then shows two distinct regions of crack growth measured using a microscope: (1) a slower and smoother crack growth region labeled as *PL0* with a length of 2.45 mm and (2) a faster and rougher crack growth region labeled as *PL1* with a length of 8.91 mm. Thus, the total experimentally determined crack length is 51.4 mm, a value only 2% greater than the theoretical prediction for the assumed fracture toughness. These regions of differing crack growth rates also evidenced by and in close correlation with the data shown in Figure 17, where it is shown that the crack growth rate dramatically increases after the crack length reaches 43 mm, which corresponds to the boundary between *PL0* and *PL1* at 42.4 mm in Figure 16.

Table 6. Loading history of Specimen 1.

Set	Date	Loading level and rate	No. of cycle	Notes
1	28-Oct	20k - 25k @ 2k/sec	300	2 AE sensors
2	28-Oct	20k - 25k @ 2k/sec	1000	
3	28-Oct	20k - 25k @ 2k/sec	1000	
4	28-Oct	20k - 28k @ 4k/sec	1000	change of loading level and loading rate
5	29-Oct	20k - 28k @ 4k/sec	1000	
6	29-Oct	20k - 28k @ 4k/sec	2000	
7	29-Oct	20k - 28k @ 4k/sec	3000	Crack first seen after 1850 cycles in this set
8	30-Oct	20k - 28k @ 4k/sec	1250	10 AE sensors
9	30-Oct	20k - 28k @ 4k/sec	2000	
10	31-Oct	20k - 28k @ 4k/sec	2000	
11	31-Oct	20k - 28k @ 4k/sec	1600	
12	31-Oct	20k - 28k @ 4k/sec	2000	
13	1-Nov	20k - 28k @ 4k/sec	2000	
14	1-Nov	20k - 28k @ 4k/sec	4000	
15	4-Nov	20k - 30k @ 5k/sec	2000	change of loading level and loading rate
16	4-Nov	20k - 30k @ 5k/sec	4000	
17	5-Nov	20k - 30k @ 5k/sec	800	Failed

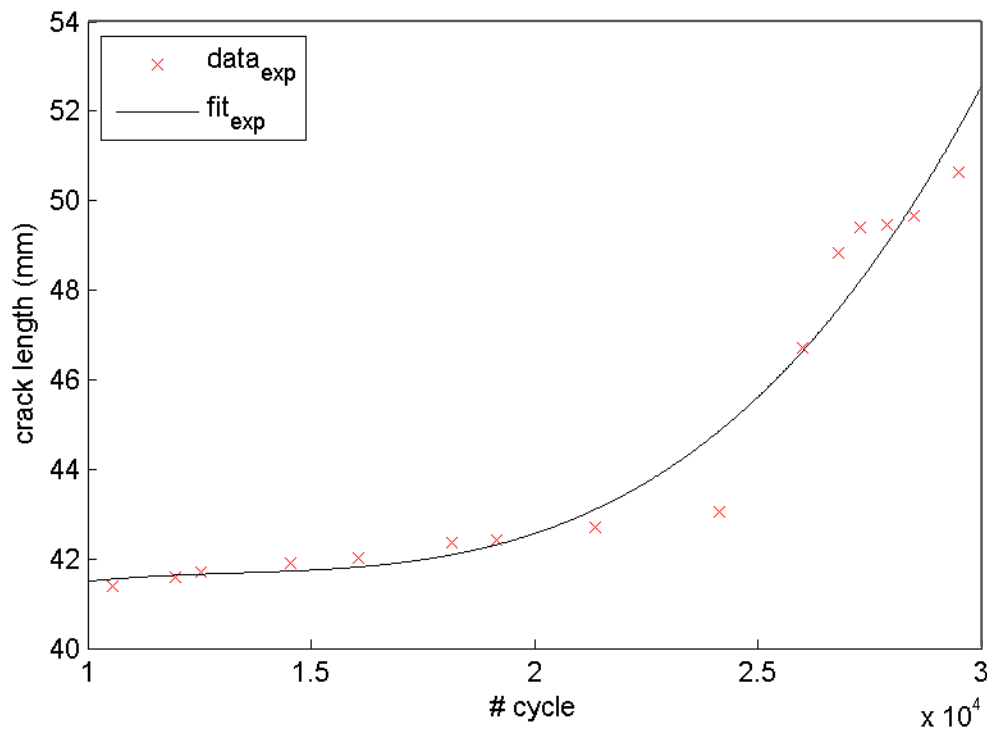**Figure 16.** Specimen 1 crack length measurements from microscope.

Figure 17. Crack growth rates observed in Specimen 1.

With the peak loading determined, the loading range was the next parameter of interest. Equation 6 shows that this is a primary variable affecting the number of cycles that would be required to produce failure, where it was desirable to minimize this number such that each test could be conducted in one week. However, in order to solve Equation 6, a value of *EIFS* must be known. One way of determining *EIFS* is through Equation 8:

$$\Delta K_{th} = \frac{\Delta P_f}{BW^{1/2}} \frac{2+\alpha}{(1-\alpha)^{3/2}} (0.886 + 4.64\alpha - 13.32\alpha^2 + 14.7\alpha^3 - 5.6\alpha^4) \qquad \textbf{(Eq. 8)}$$

Here, ΔK_{th} = threshold cyclic stress intensity factor, ΔP_f = load limit corresponding to fatigue limit, $\alpha = \frac{a_i + EIFS}{W}$, and a_i = initial crack length (length of the notch). ΔK_{th} and ΔP_f are materials properties [38]. Thus *EIFS* is also is also a material property and should be identical for all specimens made of same material. As a result, ΔK_{th} can be approximated using Equation 9,

$$\Delta K_{th} = 5.5\,\sigma_{ys}\sqrt{\bar{l}} \qquad \textbf{(Eq. 9)}$$

where σ_{ys} = yield strength of steel and l = grain size of steel [40]. Ziegler *et. al.* [41] found that ΔK_{th} of ASTM A36 steel (σ_{ys} = 60ksi and *E* = 29,000 ksi) is 3.4 MPa$\sqrt{m}$ for *R* = 0.6 and 6.4 MPa$\sqrt{m}$ for *R* = 0.1, where *R* is the ratio between the minimum and maximum applied loads. Since ΔK_{th} cannot be directly calculated from Equation 8 or 9 from the available known quantities, Ziegler et al.'s ΔK_{th} of 3.4 MPa$\sqrt{m}$ for the larger stress range of *R* = 0.6 was used along with ΔP_f = 3.0 kips to obtain an *EIFS* value of 0.449 mm (0.0176 inch). ΔP_f = 3.0 kips was selected based on the criteria for this variable that it should result in *N* from Equation 6 approaching infinity, or equating to approximately 5 million cycles.

With *EIFS* known, Equation 6 can be used to calculate *N*, which results in 3.5E6 and 6.5E6 for ΔP = 10 kips and 8 kips, respectively. As a result, ΔP = 10 kips was selected as the preferred loading range as this would result in the ability to complete each test within one week with the 0.25 Hz capability of the available testing equipment, which was generally maximized during the testing as shown in Table 6.

Crack lengths were measured using a hand-held USB microscope as illustrated by Figure 15. The same microscope was used to obtain Fig. 18 and to create the data previously shown in Table 6. An alternative method is to use the crack mouth opening displacement using Equations 10 and 11:

$$\frac{a}{W} = 1.002 - 4.063U_x + 11.2\,U_x^2 - 106.04\,11.2\,U_x^3 + 464\,U_x^4 - 650.66\,U_x^5 \qquad \textbf{(Eq. 10)}$$

$$U = \left(\left(\frac{EVB}{P}\right)^{\frac{1}{2}} + 1\right)^{-1} \ where \ 0.2 \ \leq \frac{a}{W} \geq 0.975 \qquad \textbf{(Eq. 11)}$$

where U = Crack mouth opening displacement, P = applied load, and E = Young's modulus of elasticity. A view of the specimen at the completion of testing is shown in Figure 19.
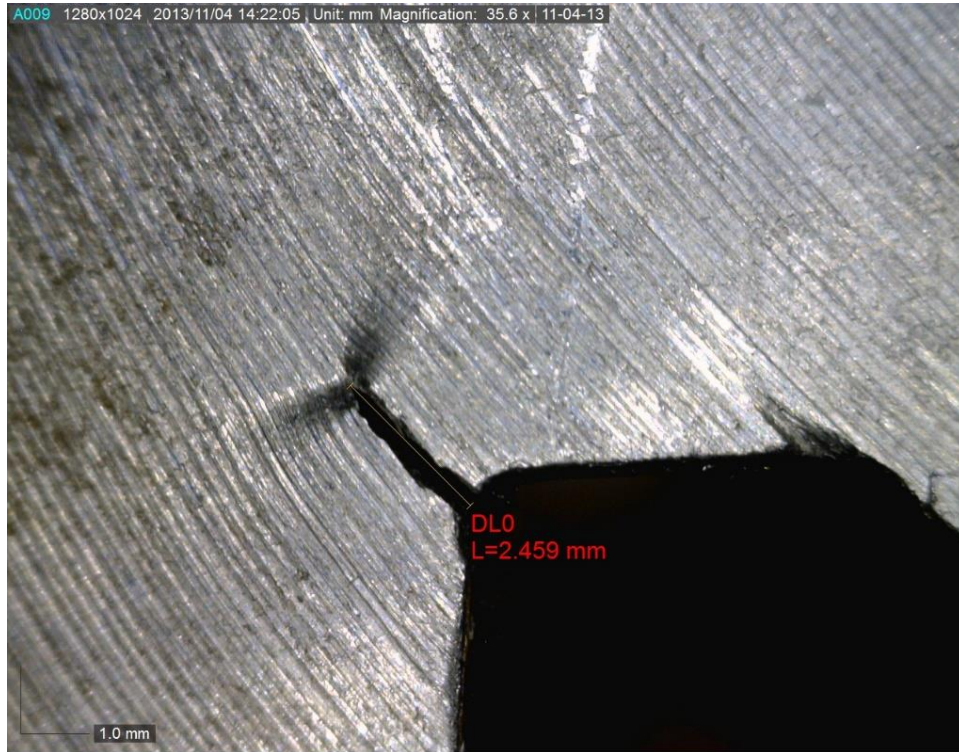
Figure 18. Crack length measurement.
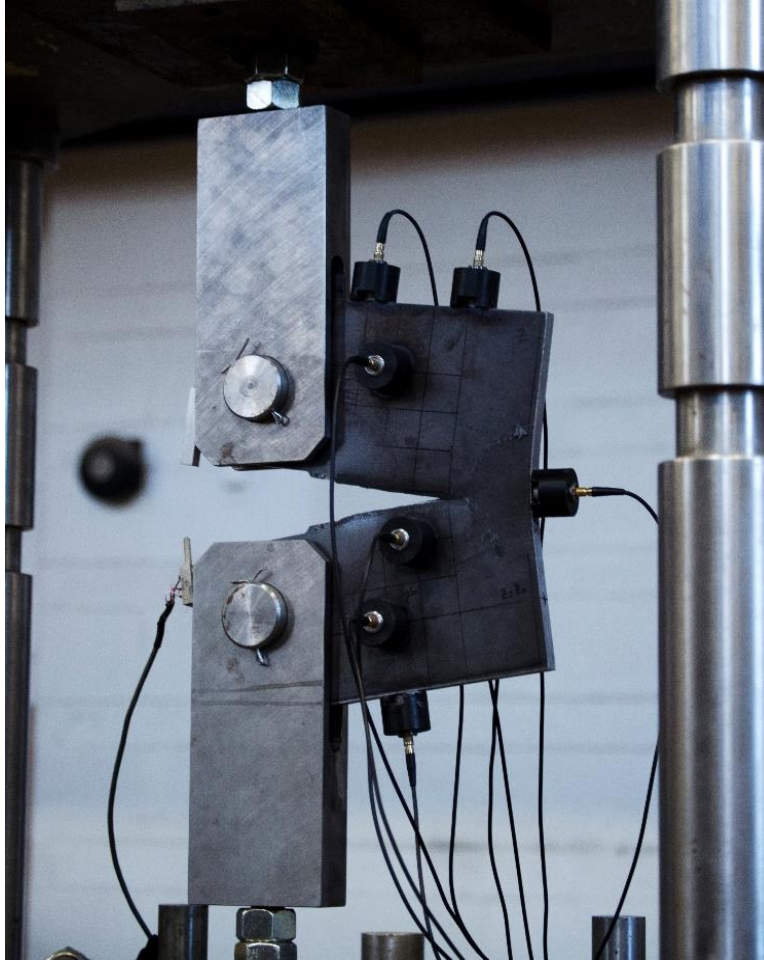
Figure 19. Specimen after fracture had occurred, at conclusion of testing.

Figure 20 shows an example of the fatigue loading during testing of Specimen 1. It can be observed that the target high and low load values are not constant over time. This can be attributed to the testing machine which was not ideally suited for this type of testing. Although less than ideal, the objective of the research, to evaluate a monitoring methodology, could still be achieved.
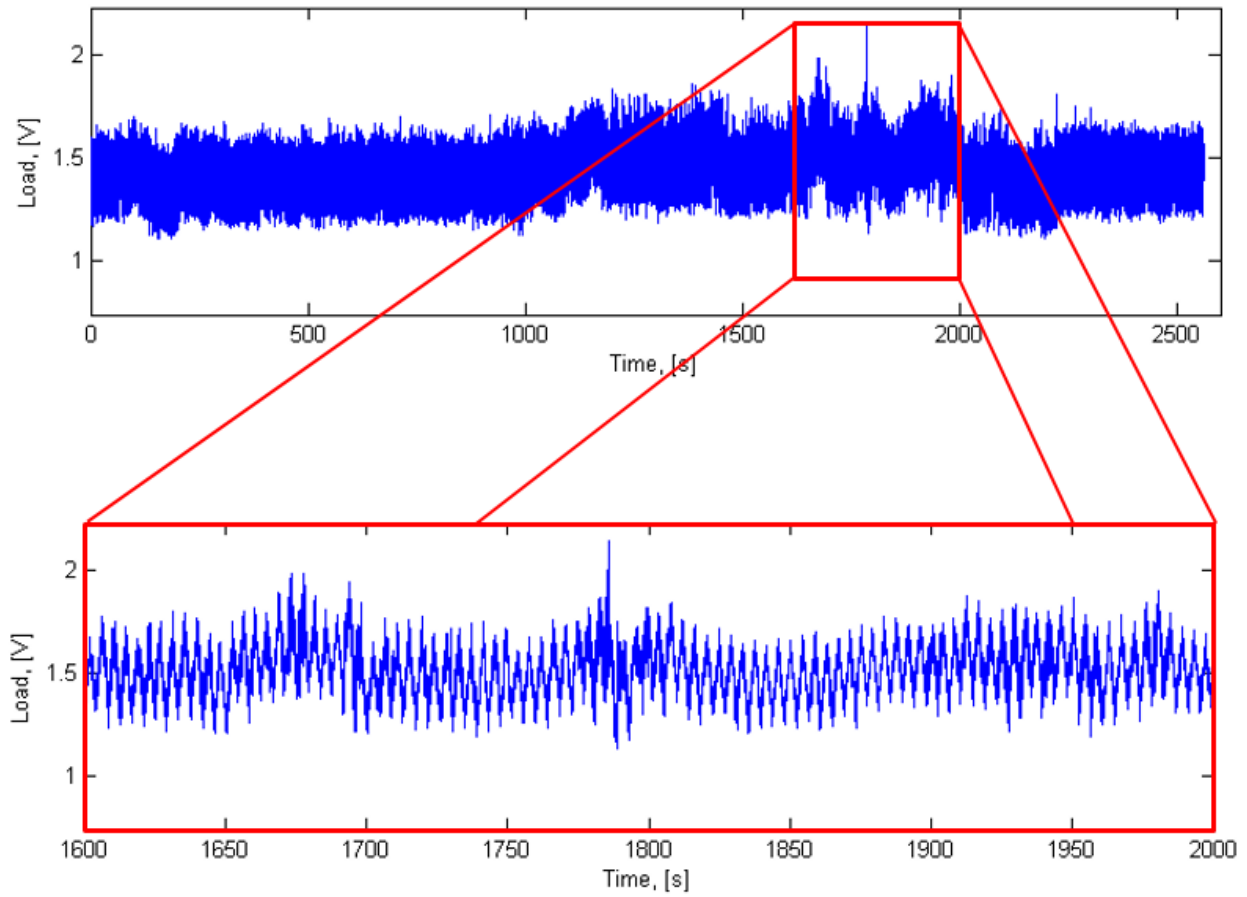
Figure 20. Example of fatigue load data from Specimen 1.

FINDINGS

In this chapter, experimental results are presented and discussed with a focus on AE.

Specimen 0

(a)

(b)

(c)
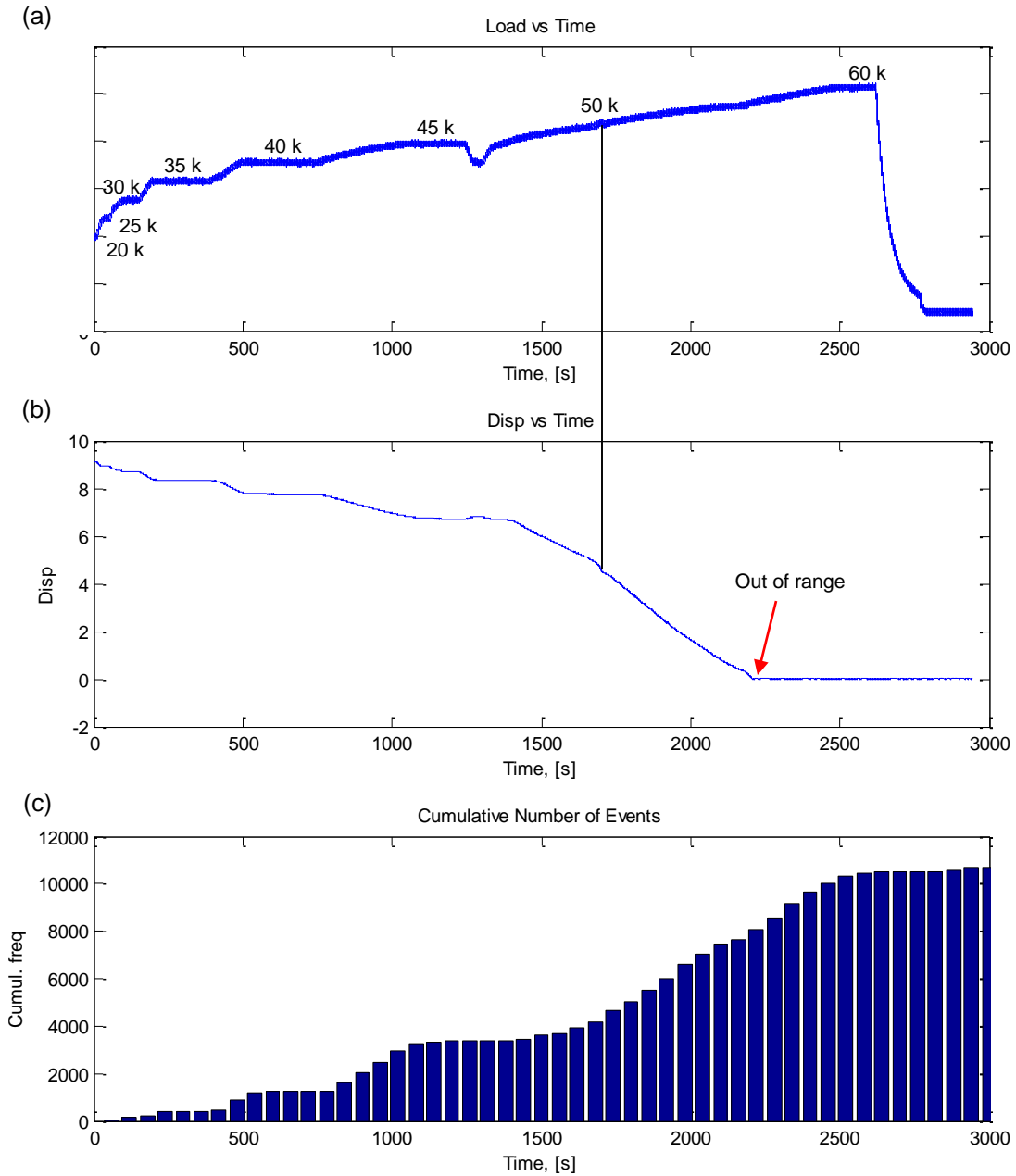
Figure 21. Collected test data: (a) Applied tension load vs. time, (b) notch opening displacement vs. time, and (c) cumulative AE events vs. time.

As can be observed from the cumulative AE events, Figure 21 (c), the rate of AE events is approximately constant. This test was discontinued at a load of 60 kips in order to avoid sudden fracture of the plate. Although there was no fatigue crack observed, many AE events were recorded. These could have two reasons: (1) noise from the experimental setup or (2) AE released from steel yield. The noise from the setup seems difficult to explain as there is no cyclic loading, which could come from friction between pins and specimen. The second explanation is yield from the crack tip. However, yield onset occurred at an applied tension force of approximately 50 kips (Figure 21 (a), (b)). Most likely, the AE events come from vibrations in the hydraulic system of the testing machine.

Specimens 1 and 2

Table 6 in Chapter *Methodology*, Section *Loading Protocols* gives a summary of the performed fatigue test on Specimen 1. For the first 7 cycle sets, only two AE sensors were employed, in order to determine data acquisition parameters under a fatigue-type loading. Crack growth measurements were taken using a digital microscope after each set of cycles and a set of examples is illustrated in Figure 22.
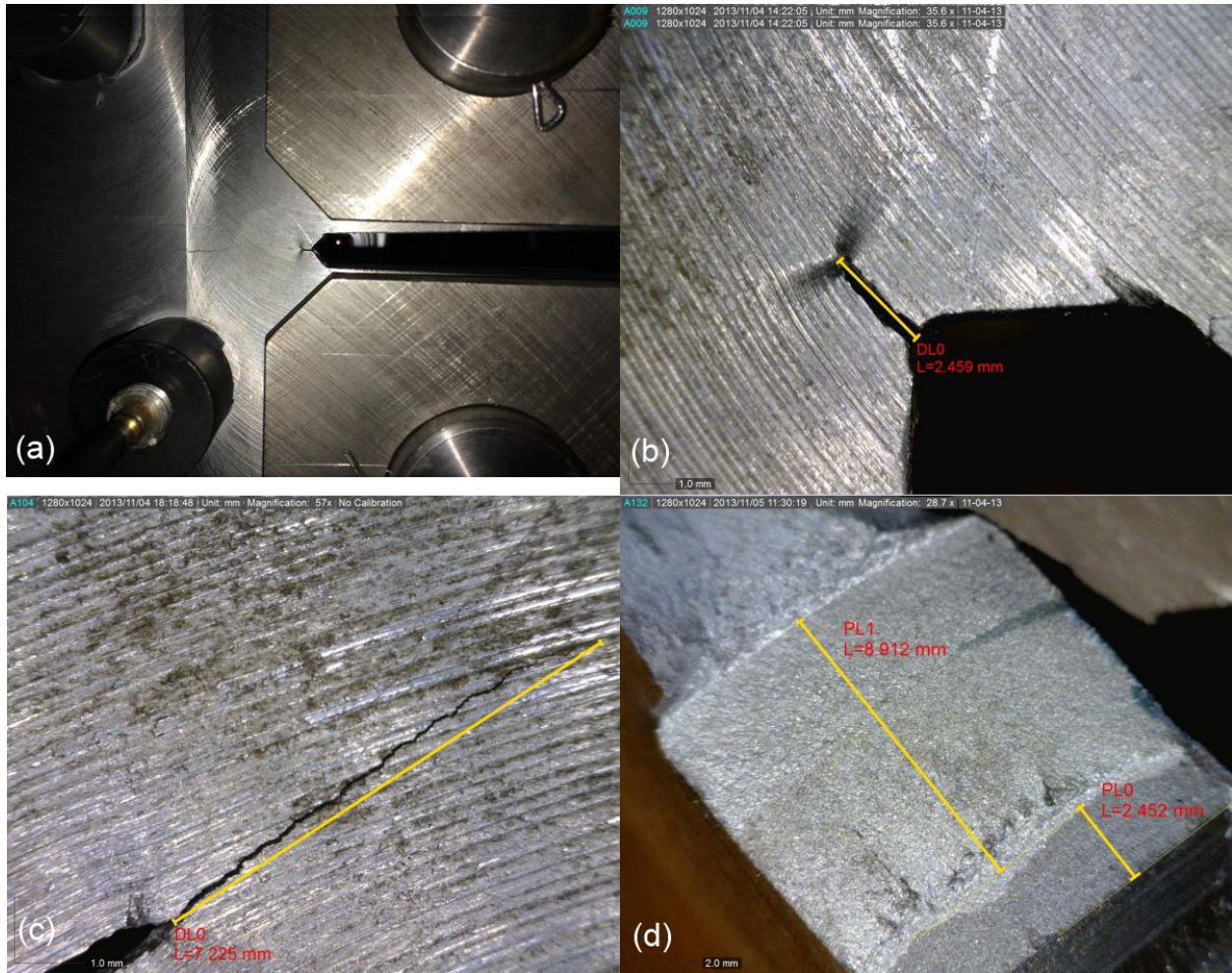
Figure 22. Examples of observed crack growth for Specimen 1: (a) After 10,550 cycles, (b) after 25,500 cycles, (c) after 28,500 cycles, and (d) after fracture had occurred, i.e. 30,950 cycles.

Similarly, Specimen 2 was tested and crack growth measured. The following sections present and discuss the recorded AE data. The following terminology is used in Tables 7 and 8:

- Total events: Total AE events recorded by data acquisition system. The threshold levels to trigger recording was set to ± 0.1 V. As soon as one of the channel in the network exceeds the threshold, all channels start recording and the event is stored.
- Real events: These were selected manually by going through all events and discard the ones that appeared to be noise. These typically consist of constant incoherent noise with no distinct *p*-wave arrival and subsequent exponential amplitude decay.
- Located events: The location of all real events was estimated but the ones that were outside of the physical boundaries of the specimen were discarded. In order to allow for some error in the prediction a volume of 2 inches around the physical boundary of the specimen was still considered part of the specimen.

- Selected MTI events: A small number of located events were selected and their MTI solution computed. The selection was subjective to include events from different regions such as the crack tip and the pins. The full solutions including detailed stereographs are included in the appendices.
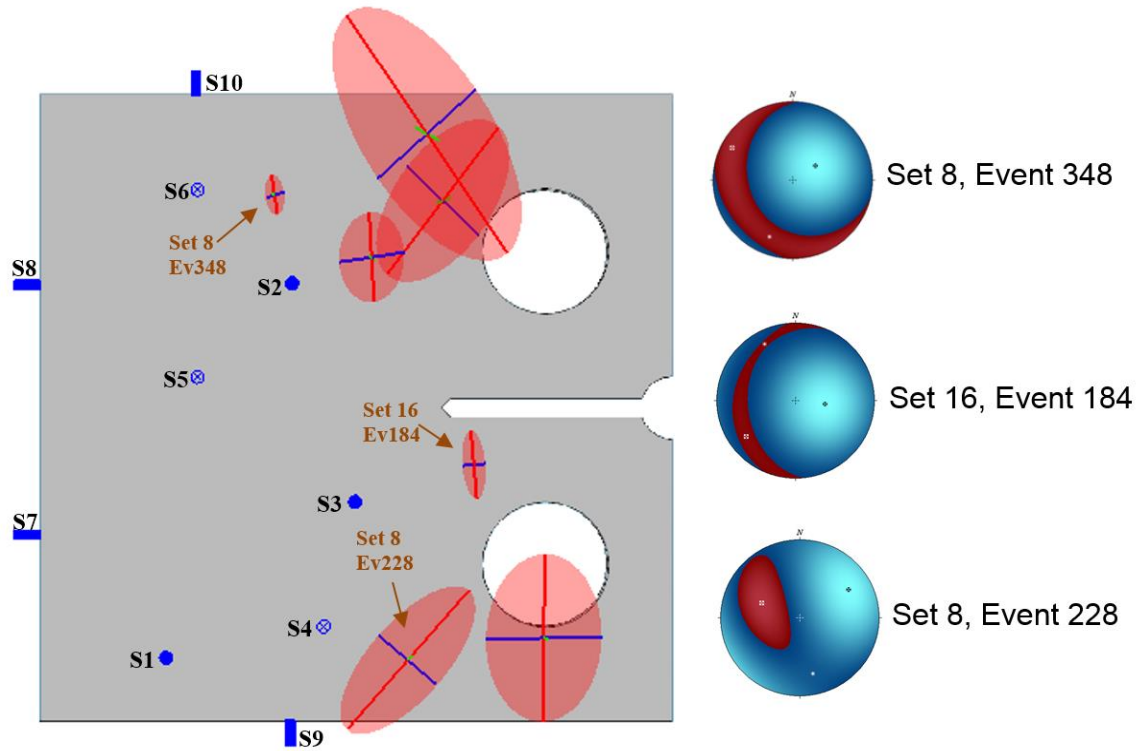
AE Results Specimen 1

As explained earlier, loading Sets 1 through 7 only had two sensors and the data was not further evaluated because it is not possible to perform a quantitative analysis (i.e. source locations, MTI) without a greater number of sensors. Table 7 summarizes the AE event data collected for the rest of the sets. It can be observed that, with increasingly more stringent requirements, the number of events decreases. This further highlights the danger of using qualitative AE techniques that do not aim at directly estimating the origin and nature of an AE signal.

Table 7. Summary of recorded AE events for Specimen 1.

Specimen 1	Set 8	Set 9	Set 10	Set 11	Set 12	Set 13	Set 14	Set 15	Set 16	Set 17
Total events	699	231	99	82	223	284	566	904	617	273
Real events	122	25	4	2	9	11	20	39	39	1
Located events	5	0	0	0	0	0	0	0	1	0
Selected MTI events	2	0	0	0	0	0	0	0	1	0

As can be seen in Figure 23, the majority of locatable events did not actually come from within proximity of the fatigue crack. However, they do seem to originate from the pins where the loads are applied. This highlights the need to evaluate a different test specimen geometry, which will be done in the future. Three events were selected for further computing the moment tensor solutions.

The selected events that were analyzed with the MTI toolbox are presented with colored stereographs. Events 184 in particular is of mixed-mode-type which corresponds to a crack-like behavior. However, the solution indicates that it is a closing crack which is difficult to explain. All of the events for Specimen 1 seem to be of implosive (or compression) type. It becomes clear that it is somewhat difficult to judge MTI solutions in isolation. All details of these solutions including error estimates can be found in Appendix A.

Figure 23. Estimated source locations and MTI beachball solutions for all sets of Specimen 1.

AE Results Specimen 2

Similarly to Specimen 1, the number of events drop significantly when the stringent requirements to locate or compute an MTI are desired. A summary of all events from Specimen 2 is shown in Table 8. Note that Set 11 has been omitted because the data acquisition did not record due to an error.

Table 8. Summary of recorded AE events for Specimen 1.

Specimen 1	Set 1	Set 2	Set 3	Set 4	Set 5	Set 6	Set 7	Set 8	Set 9	Set 10
Total events	66	124	1023	0	116	3	314	4	85	42
Real events	15	2	246	0	8	0	47	2	7	0
Located events	2	0	53	0	1	0	1	1	0	0
Selected MTI events	1	0	0	0	1	0	0	0	0	0
	Set 12	Set 13
Total events	1032	432
Real events	0	0
Located events	0	0
Selected MTI events	0	0

For Specimen 2, a few events were predicted to originate from the crack tip. Figure 24 shows all located events except the ones for Set 3 (these are presented and discussed in Figure 25). In particular, Event 25 was located with very little uncertainty and the MTI solution indicates that it is a tension-type crack that caused it. Although Event 4 has more uncertainty in its location, it still gives a reasonable MTI solution that can be explained by the crack. All details of these solutions including error estimates can be found in Appendix B.

Figure 24. Estimated source locations and MTI beachball solutions for all sets (except Set 3) for Specimen 2.
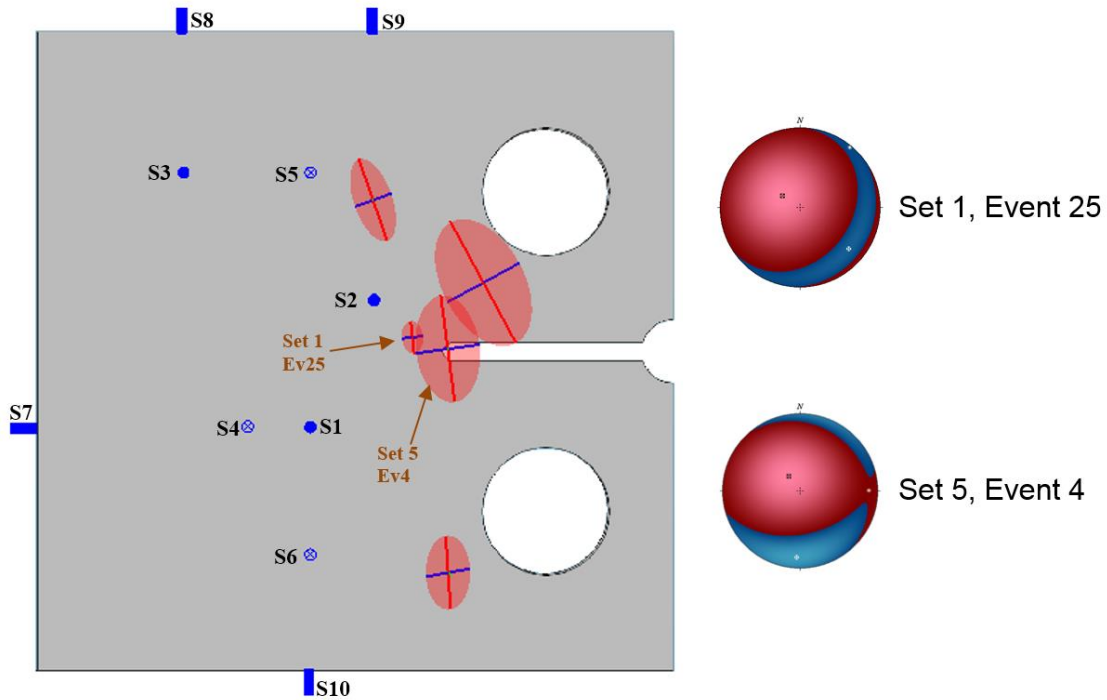
In Set 3, a large number of AE events were recorded, as presented in Table 8. Figure 25 shows the events that were locatable for Set 3. All of these seem to originate from the lower load application pin which could mean that something got stuck between the clevis and the specimen.
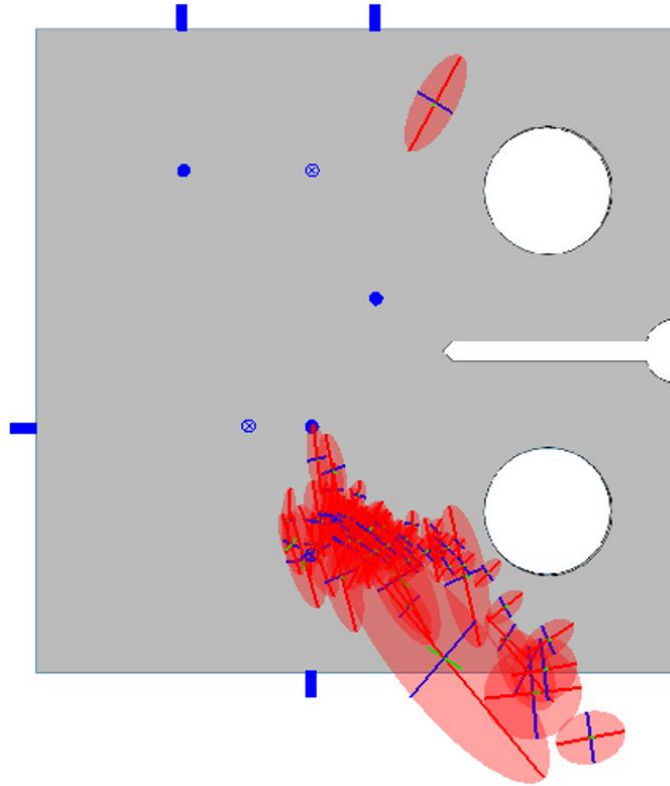
Figure 25. Estimated source locations for set 3 of Specimen 2.

Summary

Although a large number of AE events were recorded for any given set of fatigue cycles, only a few were of high enough quality to be suitable for source location estimation. From these, five were selected and processed using the MTI toolbox where an absolute MTI was performed. Since only very few AE events were locatable, it is very difficult to judge whether the MTI solutions are feasible. However, for the two events from Specimen 2, the MTI solutions correspond with the theoretically expected and observed behavior and seemed to explain the physics of the crack.

One measure of relative error that is available from the solution is the so-called condition number, κ. The higher the number, the higher the likelihood that the solution of the system of equations will give satisfactory results [23]. Unfortunately, all of the inverted solutions have relatively high condition numbers, i.e. >> 100.

From the experimental observations it is clear that noise played a major role and interfered significantly with the acquisition of AE events of interest. This can be addressed in the future, but requires designing a different setup and a utilizing a better suited testing machine.

CONCLUSIONS

A quantitative methodology based on moment tensor inversion (MTI) was implemented and applied to AE data collected during fatigue testing of two compact tension (CT) Grade A36 steel specimens. The design of the specimens as well as the test procedure followed ASTM E647 specifications [24]. The following can be concluded from the tests:

- It was possible to record a large number of AE events. However, without the ability to locate, it remains difficult if not impossible to assess whether the signals are of interest or not.
- AE source location estimates were possible for a few events but many originated from regions other than the fatigue crack, with many outside of the physical boundaries of the specimen.
- Moment tensor inversion was possible for a few selected events and, for Specimen 2, produced reasonable predictions of the source mechanisms.
- Noise from the test setup was perhaps the single greatest challenge. One of the problems is that the small size of the compact tension (CT) specimen causes the load application points to be too close to the sensor network.
- The testing machine used is not well suited for this purpose, i.e. sine-type loading is not possible and there was a lot of noise in the load signal.
- In the field it may be even more challenging or impossible to control noise and it remains to be seen how quantitative AE monitoring would perform in such an environment.

RECOMMENDATIONS

At this point, it is difficult to estimate whether quantitative AE analyses are feasible for monitoring of fatigue cracks in steel bridges. The problem of noise is, after all, not only a challenge in the laboratory, but often impossible to avoid in the field. Although we were not able to collect a significant amount of data suitable for MTI, a number of selected events produced results that seemed to explain the physics.

On the methodology side, there are several things that could be improved. First, the arrangement of the sensors could be adjusted so that the sensors are closer to the expected crack. This would also optimize the aspect ratio of the network. Secondly, the location coordinates in the y-direction could be constrained when the source location is estimated to reflect the actual specimen boundaries. Finally, the specimen dimensions should be changed. For the next set of tests, we propose the use of the tall specimen per ASTM E647 [24]. A completely new fatigue setup for a different research project is currently underway and we hope to take advantage of the knowledge gained in this research to conduct another set of tests. Once this second set of tests is performed on the tall specimen, the feasibility can be better assessed. We hope to continue to capitalize on synergistic research projects to fully complete this research.

REFERENCES

[1]   J. W. Fisher, *Fatigue and fracture in steel bridges: case studies*. New York: Wiley-Interscience, 1984.

[2]   R. J. Dexter, W. Wright, J., and J. W. Fisher, "Fatigue and Fracture of Steel Girders," *Journal of Bridge Engineering,* vol. 9, pp. 278-286, 2004.

[3]   S. Alampalli, S. R. Duwadi, R. S. Herman, D. D. Kleinhaus, K. Mahmoud, J. C. Ray, J. P. Wacker, and N. Yazdani, "Enhancing Bridge Performance," in *Bridge Workshop*, Reston, VT, 2008.

[4]   M. Al-Emrani and R. Kliger, "Fatigue prone details in steel bridges," presented at the Nordic Steel Construction Conference 2009 (NSCC 2009), Malmo, Sweden, 2009.

[5]   J. W. Fisher and S. Roy, "Fatigue of steel bridge infrastructure," *Structure and Infrastructure Engineering,* vol. 7, pp. 457-475, 2011.

[6]   M. Liu, D. M. Frangopol, and K. Kwon, "Optimization of retrofitting distortion-induced fatigue cracking of steel bridges using monitored data under uncertainty," *Engineering Structures,* vol. 32, pp. 3467-3477, 2010.

[7]   J. W. Fisher, "Distortion-Induced Fatigue Cracking in Steel Bridges," Transportation Research Board, Washington, D.C.1990.

[8]   A. S. Hartman, H. L. Hassel, C. A. Adams, C. R. Bennett, A. B. Matamoros, and S. T. Rolfe, "Effects of Cross-Frame Placement and Skew on Distortion-Induced Fatigue in Steel Bridges," *Transportation Research Record: Journal of the Transportation Research Board,* vol. 2200, pp. 62-68, 2010.

[9]   J. Crain, G. Simmons, C. R. Bennett, R. Barrett-Gonzalez, A. Matamoros, and S. Rolfe, "Development of a technique to improve fatigue lives of crack-stop holes in steel bridges," *Transportation Research Record: Journal of the Transportation Research Board,* vol. 2200, pp. 69-77, 2010.

[10]   D. L. McDowell, "An Engineering Model for Propagation of Small Cracks in Fatigue," *Engineering Fracture Mechanics,* vol. 56, pp. 357-377, 1997.

[11]   C. U. Grosse and M. Ohtsu, Eds., *Acoustic Emission Testing - Basics for Research-Applications in Civil Engineering*. Berlin & Heidelberg, Germany: Springer Verlag, 2008, p.^pp. Pages.

[12]   J. Yu and P. Ziehl, "Stable and unstable fatigue prediction for A572 structural steel using acoustic emission," *Journal of Constructional Steel Research,* vol. 77, pp. 173-179, 2012.

[13]   J. Yu, P. Ziehl, B. Zarate, and J. M. Caicedo, "Prediction of fatigue crack growth in steel bridge components using acoustic emission," *Journal of Constructional Steel Research,* vol. 67, pp. 1254-1260, 2011.

[14]   B. Zarate, J. M. Caicedo, J. Yu, and P. Ziehl, "Deterministic and probabilistic fatigue prognosis of cracked specimens using acoustic emission," *Journal of Constructional Steel Research,* vol. 76, pp. 68-74, 2012.

[15]   L. Yu, S. Momeni, V. Godinez, V. Giurgiutiu, P. Ziehl, and J. Yu, "Dual Mode Sensing with Low-Profile Piezoelectric Thin Wafer Sensors for Steel Bridge Crack Detection and Diagnosis," *Advances in Civil Engineering,* vol. 2012, pp. 1-10, 2012.

[16]   D. G. Aggelis, E. Z. Kordatos, and T. E. Matikas, "Acoustic emission for fatigue damage characterization in metal plates," *Mechnics Research Communications,* vol. 38, pp. 106-110, 2011.

[17]   F. F. Barsoum, J. Suleman, A. Korcak, and E. v. K. Hill, "Acoustic Emission Monitoring and Fatigue Life Prediction in Axially Loaded Notched Steel Specimens," *Journal of Acoustic Emission,* vol. 27, pp. 40-63, 2009.

[18]   J. McKeefrey and C. Shield, "Acoustic Emission Monitoring of Fatigue Cracks in Steel Bridge Girders," Minnesota Department of Transportation, St. Paul, Minnesota1999.

[19]   M. S. M. Zain, N. Jamaludin, Z. Sajuri, M. F. M. Yusof, and Z. H. Hanafi, "Acoustic Emission Study of Fatigue Crack Growth in Rail Track Material," presented at the National Conference in Mechanical Engineering Research and Postgraduate Studies (2nd NCMER 2010), Pahang, Malaysia, 2012.

[20]   Z. Zhu, Z. Wang, and J. Peng, "Acoustic Emission Monitoring the Fatigue Crack Growth in SM50B-Zc Steel," *Journal of Material Science and Technology,* vol. 6, pp. 345-350, 1990.

[21]   J. Takatsubo and T. Kishi, "Quantitative Acoustic Emission Source Characterization of Microcrackings in Steel," *Research in Nondestructive Evaluation,* vol. 1990, pp. 219-233, 1990.

[22]   K. Aki and P. G. Richards, *Quantitative Seismology*, 2nd ed. Sausalito, CA: University Science Books, 2002.

[23]   L. M. Andersen, "A relative moment tensor inversion technique applied to seismicity induced by mining," PhD Dissertation, Faculty of Science, University of Witwatersrand, Johannesburg, South Africa, 2001.

[24]   ASTM, "E647-11e1: Standard Test Method for Measurement of Fatigue Crack Growth Rates," ed. West Conshohocken, PA: ASTM International, 2010.

[25]   G. McLaskey and S. D. Glaser, "Acoustic Emission Sensor Calibration for Absolute Source Measurements," *Journal of Nondestructive Evaluation,* vol. 31, pp. 157-168, 2012.

[26]   J. H. Kurz, C. U. Grosse, and H.-W. Reinhardt, "Strategies for reliable automatic onset time picking of acoustic emissions and of ultrasonic signals in concrete," *Ultrasonics,* vol. 43, pp. 538-546, 2005.

[27]   L. Geiger, "Herdbestimmung bei Erdbeben aus den Ankunftszeiten," *Nachrichten von der Königlichen Gesellschaft der Wissenschaften zu Göttingen,* vol. 4, pp. 331-349, 1910.

[28]   B. Schechinger, "Schallemissionsanalyse zur Überwachung der Schädigung von Stahlbeton," PhD PhD Dissertation, Institut für Baustatik und Konstruktion, Eidgenössische Technische Hochschule (ETH) Zürich, Zurich, Switzerland, 2006.

[29]   M. Ge, "Analysis of Source Location Algorithms, Part II: Iterative methods," *Journal of Acoustic Emission,* vol. 21, pp. 29-51, 2003.

[30]   T. Schumacher, D. Straub, and C. Higgins, "Toward a probabilistic acoustic emission source location algorithm: A Bayesian approach," *Journal of Sound and Vibration,* vol. 19, pp. 4233-4245, 2012.

[31]   T. Schumacher, "Acoustic Emission Techniques Applied to Conventionally Reinforced Concrete Bridge Girders," Oregon Department of Transportation (ODOT), Salem, ORSeptember 2008.

[32] L. Mhamdi, T. Schumacher, and L. M. Linzer, "Development of Seismology-based Acoustic Emission Methods for Civil Infrastructure Applications," presented at the Review of Progress in Quantitative Nondestructive Evaluation (QNDE) Denver, CO, 2012.

[33] F. Finck, J. H. Kurz, C. U. Grosse, and H.-W. Reinhardt, "Advances in Moment Tensor Inversion for Civil Engineering," presented at the International Symposium Non-Destructive Testing in Civil Engineering (NDT-CE), 2003.

[34] ASTM, "ASTM A370-12a: Standard Test Methods and Definitions for Mechanical Testing of Steel Products," ed. West Conshohocken, PA: ASTM International, 2012.

[35] C. U. Grosse and T. Schumacher, "Anwendungen der Schallemissionsanalyse an Betonbauwerken," *Bautechnik,* vol. 90, pp. 721-731, 2013.

[36] S. A. Meguid, *Engineering Fracture Mechanics*: Elsevier Science, 1989.

[37] J. M. Barsom and S. T. Rolfe, *Fracture and Fatigue Control in Structures: Applications of Fracture Mechanics*: ASTM International, 1999.

[38] A. R. Shahani and H. M. Kashani, "Assessment of equivalent initial flaw size estimation methods in fatigue life prediction using compact tension specimen tests," *Engineering Fracture Mechanics,* vol. 99, pp. 48-61, 2013.

[39] N. E. Dowling, K. S. Prasad, and R. Narayanasamy, *Mechanical Behavior of Materials: Engineering Methods for Deformation, Fracture, and Fatigue*. Upper Saddle River, NJ: Prentice Hall, 1999.

[40] G. R. Yoder, L. A. Cooley, and T. W. Crooker, "A critical analysis of grain-size and yield-strength dependence of near-threshold fatigue crack growth in steels," presented at the Fracture Mechanics: Fourteenth Symposium, Los Angeles, USA, 1983.

[41] B. M. Ziegler, J. W. Shaw, T. S. Cordes, D. J. Lingenfelser, and J. C. J. Newman, "Fatigue Crack Growth Rate Behavior of A36 Steel Using ASTM Load-Reduction and Compression Precracking Test Methods," *Journal of ASTM International,* vol. 9, 2012.

APPENDIX A: MOMEN TENSOR SOLUTIONS SPECIMEN 1
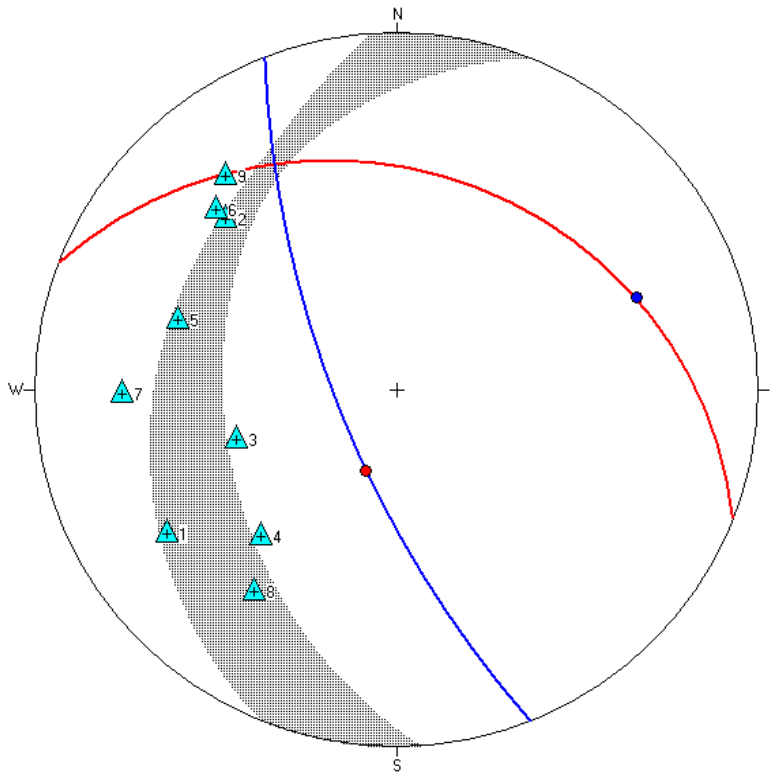
EventID: 184

Absolute MTI

Rotate from [N,E,D] --> [N,E,D]
Fault Plane Solution
(strike,dip,rake) in degrees
   Plane 1: (290.9, 27.2, -134.1)
   Plane 2: (158.4, 70.8, -70.3)
Source parameters
   Trace = -1.54828004743184E18
   %ISO = -31.2%
   %DC = 4%
   Deviation DC = 0.47
   R ratio = -41.7
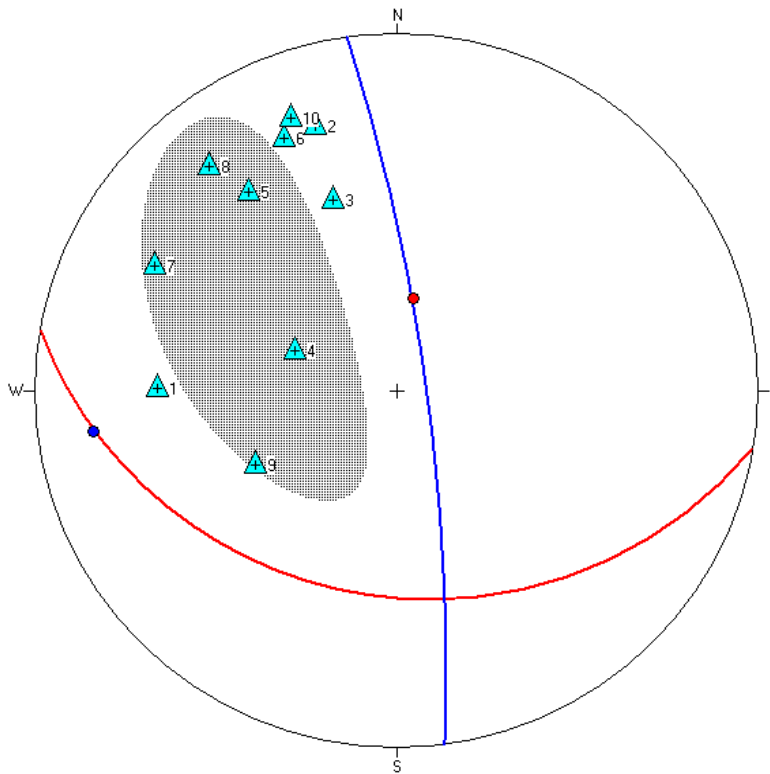   Coseismic Vol. Change = -9498651m3
Solution parameters
   No. Equations = 9
   Condition No. = 19072
   Ratio (StdErr/ScalarMoment) = 0

List of Symbols:
▽ Station above source
△ Station below source
+ ● P-wave away from source
– ○ P-wave towards source

EventID: 228

Absolute MTI

Rotate from [N,E,D] --> [N,E,D]
Fault Plane Solution
(strike,dip,rake) in degrees
   Plane 1: (99.5, 29.5, 19.6)
   Plane 2: (352.2, 80.4, 118.1)
Source parameters
   Trace = -9.1372165047255E16
   %ISO = -26.6%
   %DC = 47.9%
   Deviation DC = 0.26
   R ratio = -39.8
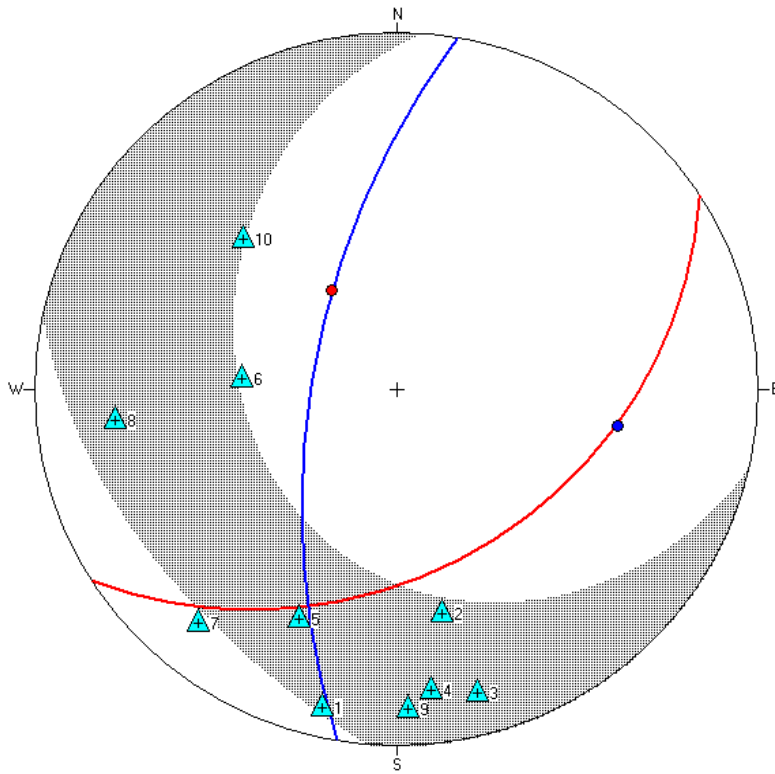   Coseismic Vol. Change = -560565.43m3
Solution parameters
   No. Equations = 10
   Condition No. = 2040.6
   Ratio (StdErr/ScalarMoment) = 0

List of Symbols:
▽ Station above source
△ Station below source
+ ● P-wave away from source
– ○ P-wave towards source

EventID: 348
Absolute MTI

Rotate from [N,E,D] --> [N,E,D]
Fault Plane Solution
(strike,dip,rake) in degrees
    Plane 1: (57.1, 36.6, -48.6)
    Plane 2: (189.5, 63.3, -116.1)
Source parameters
    Trace = -3.79746027466392E17
    %ISO = -20.7%
    %DC = 6.9%
    Deviation DC = 0.46
    R ratio = -35.1
    Coseismic Vol. Change = -2329730.25m3
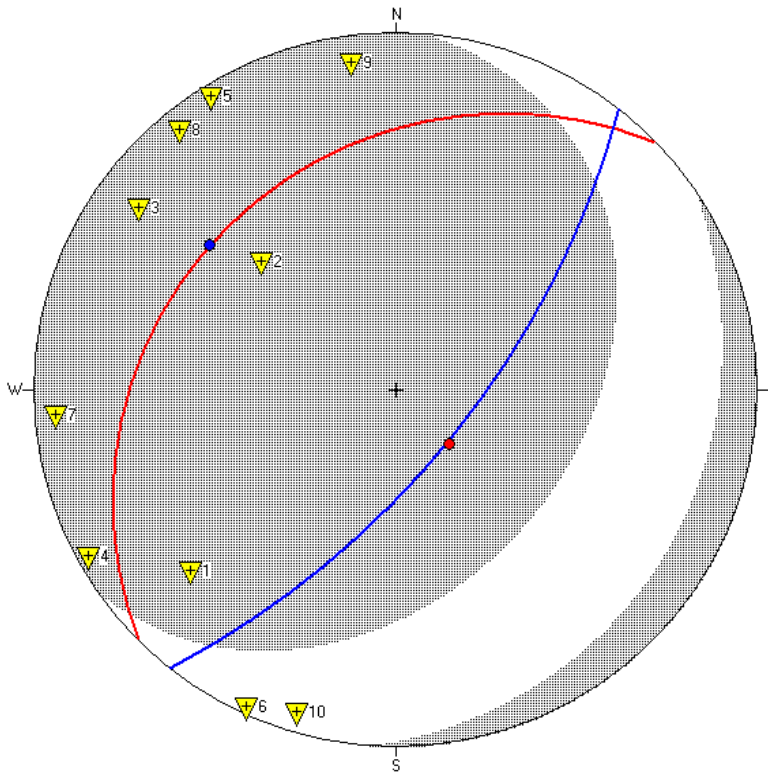Solution parameters
    No. Equations = 10
    Condition No. = 2123.2
    Ratio (StdErr/ScalarMoment) = 0

List of Symbols:
▽ Station above source
△ Station below source
+ ● P-wave away from source
− ○ P-wave towards source

APPENDIX B: MOMENT TENSOR SOLUTIONS SPECIMEN 2

EventID: 25
Absolute MTI

Rotate from [N,E,D] --> [N,E,D]
Fault Plane Solution
(strike,dip,rake) in degrees
   Plane 1: (225.6, 23.6, 96.6)
   Plane 2: (38.4, 66.5, 87)
Source parameters
   Trace = 2.83966882376057E17
   %ISO = 28.1%
   %DC = 6.2%
   Deviation DC = 0.46
   R ratio = 39.8
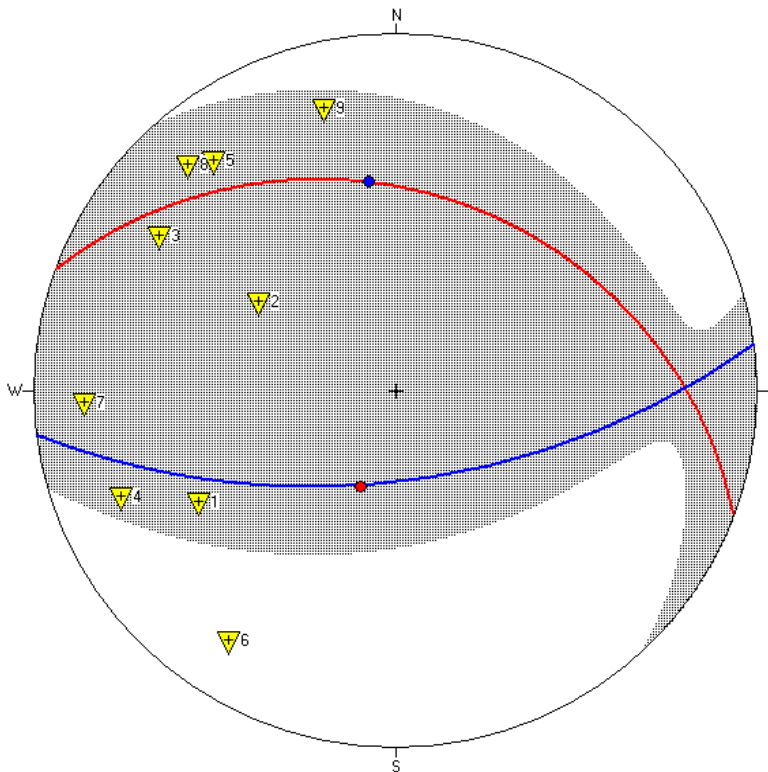   Coseismic Vol. Change = 1742128.12m3
Solution parameters
   No. Equations = 10
   Condition No. = 254887.7
   Ratio (StdErr/ScalarMoment) = 0

List of Symbols:
▽ Station above source
△ Station below source
+ ● P-wave away from source
− ○ P-wave towards source

EventID: 4
Absolute MTI

Rotate from [N,E,D] --> [N,E,D]
Fault Plane Solution
(strike,dip,rake) in degrees
   Plane 1: (290, 31.7, 113.7)
   Plane 2: (82.6, 61.2, 76)
Source parameters
   Trace = 5.5250996166656E16
   %ISO = 18.3%
   %DC = 34.3%
   Deviation DC = 0.32
   R ratio = 33.8
   Coseismic Vol. Change = 338963.15m3
Solution parameters
   No. Equations = 9
   Condition No. = 16159.4
   Ratio (StdErr/ScalarMoment) = 0

List of Symbols:
▽ Station above source
△ Station below source
+ ● P-wave away from source
− ○ P-wave towards source